AD-A119 876 IOWA UNIV IOWA CITY DEPT OF PHYSICS AND ASTRONOMY F/G 8/14
SHORT WAVELENGTH ELECTROSTATIC WAVES IN THE EARTH'S MAGNETOSHEA--ETC(U)
JUL 82 D L GALLAGHER N00014-76-C-0016
UNCLASSIFIED U OF IOWA-82-21 NL

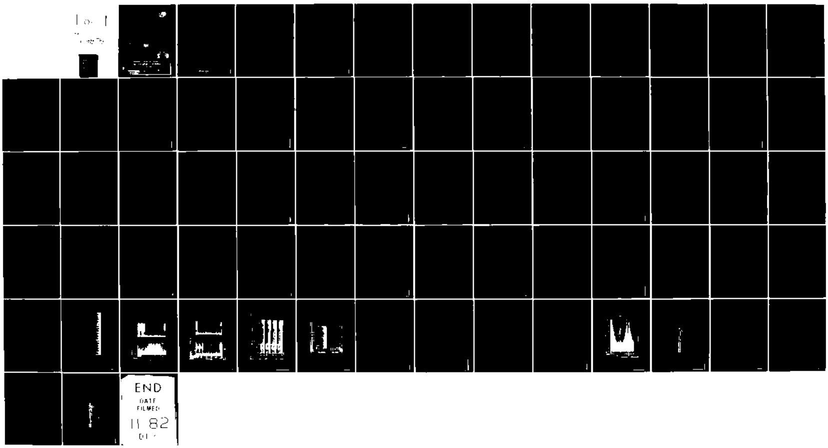

U. of Iowa 82-21

AD A119875

DTIC
ELECTE
S D
D

Department of Physics and Astronomy

THE UNIVERSITY OF IOWA

FILE COPY

U. of Iowa 82-21

SHORT WAVELENGTH ELECTROSTATIC WAVES IN THE EARTH'S MAGNETOSHEATH

by

D. L. Gallagher

July, 1982

Department of Physics and Astronomy
The University of Iowa
Iowa City, Iowa 52242

Submitted to Journal of Geophysical Research

This work was supported by the National Aeronautics and Space Administration through Contracts NAS5-20093 and NAS5-26819 with Goddard Space Flight Center, Grants NGL-16-001-002 and NGL-16-001-043 with NASA Headquarters, and the Office of Naval Research.

UNCLASSIFIED

SECURITY CLASSIFICATION OF THIS PAGE (When Data Entered)

REPORT DOCUMENTATION PAGE		READ INSTRUCTIONS BEFORE COMPLETING FORM
1. REPORT NUMBER U. of Iowa 82-21	2. GOVT ACCESSION NO. AD-A119 875	3. RECIPIENT'S CATALOG NUMBER
4. TITLE (and Subtitle) SHORT WAVELENGTH ELECTROSTATIC WAVES IN THE EARTH'S MAGNETOSHEATH		5. TYPE OF REPORT & PERIOD COVERED Progress July 1982 6. PERFORMING ORG. REPORT NUMBER
7. AUTHOR(s) D. L. Gallagher		8. CONTRACT OR GRANT NUMBER(s) N00014-76-C-0016
9. PERFORMING ORGANIZATION NAME AND ADDRESS Department of Physics and Astronomy The University of Iowa Iowa City, Iowa 52242		10. PROGRAM ELEMENT, PROJECT, TASK AREA & WORK UNIT NUMBERS
11. CONTROLLING OFFICE NAME AND ADDRESS Office of Naval Research Electronics Program Office Arlington, Virginia 22217		12. REPORT DATE July, 1982 13. NUMBER OF PAGES 53
14. MONITORING AGENCY NAME & ADDRESS (if different from Controlling Office)		15. SECURITY CLASS. (of this report) UNCLASSIFIED 15a. DECLASSIFICATION/DOWNGRADING SCHEDULE

16. DISTRIBUTION STATEMENT (of this Report)

Approved for public release; distribution is unlimited.

17. DISTRIBUTION STATEMENT (of the abstract entered in Block 20, if different from Report)

18. SUPPLEMENTARY NOTES

Submitted to JOURNAL OF GEOPHYSICAL RESEARCH, July 1982.

19. KEY WORDS (Continue on reverse side if necessary and identify by block number)

Electrostatic Waves
Magnetosheath

20. ABSTRACT (Continue on reverse side if necessary and identify by block number)

(See page following.)

DD FORM 1 JAN 73 1473 EDITION OF 1 NOV 65 IS OBSOLETE
S/N 0102-LF-014-6601

SECURITY CLASSIFICATION OF THIS PAGE (When Data Entered)

ABSTRACT

Recent observations with the ISEE-1 spacecraft have found electric field emissions in the dayside magnetosheath whose frequency spectrum is modulated at twice the spacecraft spin period. The upper frequency cutoff in the frequency-time spectrum of the emissions has a characteristic parabola shape or "festoon" shape. The low frequency cutoff ranges from 100 Hz to 400 Hz, while the high frequency limit ranges from about 1 kHz to 4 kHz. The bandwidth is found to minimize for antenna orientations parallel to the wave vectors. The wave vector does not appear to be related to either the local magnetic field direction or the plasma flow velocity. The spacecraft observed frequency spectrum results from the spacecraft antenna response to the Doppler shifted wave vector spectrum which exists in the plasma. Imposed constraints on the plasma rest-frame wave vectors and frequencies indicate that the emissions occur within the frequency range from about 150 Hz to 1 kHz, with wavelengths between about 30 meters and 600 meters. These constraints strongly suggest that the festoon-shaped emissions are ion-acoustic waves. The small group velocity and k direction of the ion-acoustic mode are consistent with wave generation upstream at the bow shock and convection downstream to locations within the outer dayside magnetosheath.

- A -

I. INTRODUCTION

Wideband electrostatic noise is a general description of all low frequency electrostatic waves which are characterized by a wide spectrum of frequencies. Waves of this nature are found at low altitudes in the auroral regions [Kintner, 1976], in the Earth's distant magnetosphere on auroral field lines [Gurnett and Frank, 1977], at boundary layers such as the plasma sheet boundary layer in the magnetotail [Gurnett et al., 1976], and in the dayside magnetosheath [Rodriguez and Gurnett, 1975; Rodriguez, 1979]. Most forms of broadband electrostatic waves appear to be associated with field-aligned current or turbulent processes and usually do not possess any discrete features in frequency-time spectrograms. The absence of discrete spectral features makes it difficult to associate the spectrum with a particular wave mode. Usually plasma wave emissions are identified with a discrete frequency such as the electron plasma frequency or found to possess a well-defined upper or lower frequency cutoff as in the case of continuum radiation [Gurnett and Shaw, 1973]. The waves which are studied in this paper are electrostatic, broadband in frequency, and are found in the outer magnetosheath at frequencies from a few Hz to several kHz. They are unique, however, in that they possess discrete spectral features. The observation of these waves was first published by Anderson et al. [1982]. Anderson described the frequency-time spectrograms of these waves to be like "garlands hanging . a curve" or "festoon-shaped". The upper frequency cutoff in the frequency-time spectrum of the emissions has a characteristic parabola shape, analogous to a ribbon hanging in a curve. Figure 1 shows an example of the festoon-shaped emissions. This figure shows a frequency versus time spectrogram of electric fields from the ISEE-1 wideband receiver. The darker shaded regions correspond to higher electric field intensities. The characteristic rise and fall of the upper cutoff frequencies of the emission is the feature referred to as a festoon. As will be discussed, the festoon-shaped modulation of the upper cutoff frequency is directly related to the rotation of the spacecraft.

The purpose of this work is to examine the observed wave characteristics and to extend that information to a description of the wave environment and origins. First, restrictions on the possible wave number-frequency spectrum of the waves in the plasma frame of reference are inferred by model-fitting the antenna response. Wave polarization can be determined when the wave intensity is modulated in amplitude by the rotation of the dipole antenna used in the observation [Gurnett et al., 1976]. For an emission characterized by a single wavelength larger than the dipole antenna, the antenna response is sinusoidal with its rotation. When a spectrum of wave numbers ($k = 2\pi/\lambda$) is present with wavelengths comparable to the antenna length, the antenna response is more complex and information can be obtained on the wave number spectrum from the antenna response. Next, cold plasma wave modes [Stix, 1962] and hot plasma wave modes [Krall and Trivelpiece, 1973] are examined as candidates for explaining the "festoon-shaped" modulation. Plasma wave modes are evaluated on the basis of satisfying the restrictions imposed by by antenna response modeling and the plasma environment of the spacecraft. Finally, the possible origins of these emissions are discussed. Wave generation at locations within the magnetosheath and at the bow shock are considered.

This study uses data acquired by the International Sun-Earth Explorer Satellites (ISEE) 1 and 2. These spacecraft are in highly ellipical orbits inclined at about 30 degrees to the ecliptic plane, with an apogee near 22.5 R_E. The measurements from the ISEE-1 spacecraft which are used here are made with the 215 meter fine wire electric dipole antenna. The antenna oriented is normal to the spin axis of the spacecraft. The antenna rotates in a plane referred to as the spin plane which is essentially coplanar with the solar ecliptic plane. The antenna and spacecraft rotate with a 3-second period. ISEE-2 electric field measurements are made with the 30 meter fine wire electric dipole antenna. The ISEE-2 spacecraft also spins with a rotation period of 3 seconds. The antenna spin-plane of ISEE-2 is essentially the same as that of ISEE-1. Detailed information about the plasma wave instruments on board the ISEE-1 and ISEE-2 spacecrafts can be found in Gurnett et al. [1978].

II. CHARACTERISTICS OF FESTOON-SHAPED EMISSIONS

A. Frequency Versus Time Characteristics

The basic characteristics of the festoon-shaped emissions are illustrated in Figures 2 and 3. In Figure 2, 15 seconds of data from the wideband instrument on ISEE-1 are shown. The bottom panel presents data from the 1 kHz bandwidth channel and the upper panel is from the 10 kHz bandwidth channel. One complete spacecraft rotation occurs from 9:57:06 UT to 9:57:09 UT in Figure 2. During this time the bandwidth of the wave spectrum appears to maximize at about 6, 7.5, and 9 seconds. The lower panel in Figure 2 more clearly shows the frequency structure below 1 kHz. At these frequencies, the main emission appears to fall and rise in frequency. For these times in Figure 2, the lower frequency cutoff of the emission band varies from 200 Hz to 600 Hz. The upper frequency cutoff of the emission band varies from about 700 Hz to 2 kHz. Figure 3(a) shows slightly different features. At approximately 20.5 seconds and 22.0 seconds, a dropout in intensity appears at all frequencies. Just before and just after these times the bandwidth is maximized. At the minima in the bandwidth of the main emission, a second distinct frequency component appears in the spectrum. The second frequency component, however, appears at sporadic times with respect to the main frequency-time structure. The band of emissions in Figure 3(a) is seen to extend as high as about 5 kHz and perhaps lower than 200 Hz.

Figure 3(b) is similar to Figure 3(a) and shows the additional event times that are examined in more detail below.

Four channels of spectrum analyzer electric field measurements for a typical ISEE-1 pass through the magnetosphere are shown in Figure 4. The bow shock encounter at about 0900 UT is characterized by a sharp increase in wave intensity in all four frequency channels. Festoon-shaped waves begin at the bow shock encounter and extend with decreasing amplitude into the magnetosheath, downstream of the shock. The event chosen for analysis extends from 0957 UT to 1000 UT (indicated by arrow). During this time, the spectral power falls off rapidly with increasing frequency, up to as high as perhaps 10 kHz.

B. Electric to Magnetic Field Ratio

Although magnetic fluctuations exist at the selected event times, the frequency range of the fluctuations is limited to the frequency range from 5.6 Hz to 311 Hz. In the frequency range of the festoon-shaped electric field spectrum the magnetic field strength is below the instrument noise level. In a plasma, the ratio of magnetic field strength to electric field strength, cB/E, gives the local index of refraction (n) for electromagnetic waves for propagation parallel to the magnetic field. The ratio can be used to test the electrostatic character of a wave. If $cB/E \ll n$, the wave may be considered to be electrostatic. The measured value of cB/E at about 600 Hz is 4.5. Because the magnetic field strength is at the instrument noise level, the measured value of the ratio is equal to or greater than its true value. The index of refraction may be computed for whistler mode waves

[Stix, 1962], for example, using the plasma density and field values from Appendix A and propagation along the magnetic field. At a frequency of 600 Hz, the index of refraction is about 40. The measured value of cB/E is, therefore, too small to be consistent with cold plasma whistler mode waves. Only near the resonance cone does the ratio cB/E become small for an electromagnetic wave. Even when this happens the wave is approximately electrostatic. Consequently, these waves are thought to be effectively electrostatic.

C. Spectral Structure Versus Antenna Orientation

To fully understand the relationship between the antenna orientation and the observed spectral characteristics, it is first useful to review the characteristic directions that can exist in these observations. Only two directions are relevant to the analysis of these data: the local magnetic field direction and the plasma flow direction. These directions are summarized in Appendix A. The plasma flow vector is obtained from the quadrispherical LEPEDEA instrument on ISEE-1 [Frank et al., 1978]. This vector is the result of a first moment calculation over the observed particle distribution in the proton energy range 215 eV to 45 keV. Although the calculation of velocity was made over an 8-minute interval of time, the preceding and following velocity calculations differ by no more than ±2% in magnitude and less than ±2° in direction. The average plasma flow velocity is therefore fairly constant. The magnetic field vector is obtained from the Russell experiment as presented in the ISEE A and B data pool tapes described in Ogilvie and Banks [1977], with no more than a ±4% change in magnitude and less than a ±10° change in direction for measurements on either side of the selected time. It also appears to be nearly constant. The plasma flow is primarily anti-sunward. The direction and magnitude is consistent with the spacecraft location just inside the bow shock. The magnetic field is northward and in the dusk direction, consistent with the spacecraft location north of the ecliptic plane and at pre-noon local times.

The correspondence between spectral features in the wideband data and spacecraft antenna orientation is shown in Figure 5. In the lower panel, antenna orientation is plotted with respect to the spacecraft-sun line (solid line), the spin-plane projected magnetic field direction (short dashed line), and the projected plasma flow direction (long dashed line). In this figure, vertical reference lines are drawn showing the antenna direction when the emission bandwidth is maximized (time of symmetry in the periodic spectral structure). As can be seen, the antenna at the reference points is neither parallel nor perpendicular to the local magnetic field. Nor does the spectral structure appear simply related to the plasma flow direction. For the times marked by the vertical lines in Figure 5 and at the equivalent times for the data in Figures 2 and 3(a), the antenna orientation to the plasma flow and magnetic field directions are summarized in Figure 6. For the group of points corresponding to each spectrogram, the spread in angle is small. For Figure 2, the magnetic field angle is 104 ± 3 degrees, for Figure 3(a) it is 121 ± 4 degrees, and for Figure 5 (or Figure 3(b)) it is 77 ± 4 degrees. Between these times, however, the orientation angle varies significantly. The orientation angle for those times when the bandwidth is a maximum was found to vary erratically between 0° and 90° over an 8-minute time interval, which included 242 festoon events. No systematic variation or relationship of the antenna orientation to the local magnetic field or plasma flow directions was found.

Upon reexamination of the wideband data, such as found in Figures 2 and 3, it is apparent that the specific spectral shape under study is not seen continuously. It occurs for 6 to 10 seconds at a time, separated either by intervals of spectrally diffuse wideband noise or a momentary loss of the characteristic spectral shape. It seems that each period during which the festoon-shaped modulation occurs is a separate and perhaps localized event. Given the measured plasma flow of about 160 km/s, the events are localized in regions that are from 760 km to 1600 km in spatial size. This sporadic occurrence of festoon-shaped emissions was also reported by Anderson et al. [1982], where the occurrence was correlated to low frequency magneto-acoustic waves. Tsurutani et al. [1982] has most recently identified those low frequency-long wavelength magnetohydrodynamic structures as non-oscillatory "waves" generated by the drift mirror instability. The festoon-shaped events were observed during the high magnetic field and low density phase of these magnetohydrodynamic structures.

D. Region of Occurrence

The events which have been found begin at the bow shock and extend inward to locations which approach the magnetopause, i.e., within the outer magnetosheath. Events are found on the dayside of the Earth, from 6 hours to 18 hours magnetic local time. It will be shown that the frequency-time character of these emissions is a consequence of the polarization of the observed waves and the antenna pattern for varying wavelengths. Because the festoon shape of the emission is a consequence of the dipole antenna and emission polarization and not magnetosheath location, a single interval of observations will be studied in detail and used to develop an understanding of the observed frequency-time structure.

III. ANTENNA RESPONSE

The previous sections discussed the observational characteristics of the festoon-shaped spectrograms. The relationship of the festoon-shape feature to the rotation of the spacecraft is strong evidence that the spacecraft antenna is influencing the detection of the broadband electric field emissions in the magnetosheath. Before the emission spectrum can be examined, it is first necessary to derive an expression giving the antenna response to a wave in the plasma. This derivation is done in the following sections. When the antenna response is known, it will be used with the observed spectrum to deduce constraints on the true emission spectrum.

A. Antenna Response Derivation

From Maxwell's equations, the electric field in a system is given by

$$\vec{E} = -\nabla\phi - \frac{1}{c}\frac{\partial\vec{A}}{\partial t} \qquad (1)$$

Because the observed waves have no magnetic component so that $\frac{\partial\vec{A}}{\partial t} = 0$, the above expression reduces to

$$\vec{E} = -\nabla\phi \quad . \qquad (2)$$

This relation can be re-expressed as an integral along the line element $\vec{ds}$

$$\phi = -\int \vec{E} \cdot \vec{ds} \tag{3}$$

The potential difference between two points can be found by performing the integration along the line between the points. The wave is assumed to be a plane wave, where the vector components are in general complex.

$$\vec{E} = (E_x \hat{x} + E_y \hat{y} + E_z \hat{z}) e^{i(\vec{k} \cdot \vec{r} - \omega t)} \tag{4}$$

For electrostatic waves, the time origin can be chosen such that the electric field vector components are purely real. Also, the electric field and wave number vectors are parallel. The integral over a distance $\vec{\ell}$ along the antenna then takes the form

$$\phi(\ell,t) = -\int_{-\vec{\ell}/2}^{\vec{\ell}/2} (E_x \hat{x} + E_y \hat{y} + E_z \hat{z}) \cdot (\cos\theta \hat{x} dx + \sin\theta \hat{y} dy) e^{i(\vec{k} \cdot \vec{r} - \omega t)} \tag{5}$$

where θ is the orientation angle of the antenna (see Figure 7 for a sketch of the vector orientations and angle definitions). In cylindrical coordinates, after taking the dot product, using

$$\hat{x} = \hat{\rho} \cos\theta - \hat{\theta} \sin\theta,$$

$$\hat{y} = \hat{\rho} \sin\theta + \hat{\theta} \cos\theta,$$

$$\hat{z} = \hat{z},$$

where $\hat{\rho}$ and $\hat{\theta}$ are unit vectors in cylindrical coordinates, Equation 5 becomes

$$\phi(\ell,t) = -\int_{-\ell/2}^{\ell/2} (E_x \cos\theta + E_y \sin\theta) d\rho \; e^{i(\vec{k}\cdot\vec{\rho} - \omega t)} \quad . \tag{6}$$

After integration, Equation 6 becomes:

$$\phi(\ell,t) = -2(\vec{E}\cdot\hat{\ell}) \frac{\sin(k'_\rho \frac{\ell}{2})}{k'_\rho} e^{-i\omega t} \quad , \tag{7a}$$

where $\hat{\ell}$ is a unit vector along the antenna,

$$\vec{E}\cdot\hat{\ell} = E_x \cos\theta + E_y \sin\theta, \text{ and}$$

$$k'_\rho = k_x \cos\theta + k_y \sin\theta, \tag{7b}$$

is the component of the $\vec{k}$ vector along the antenna axis. The sin x/x term in Equation 7a is a standard radio interferometer pattern [Kraus, 1966]. Equation 7a can be simplified somewhat by noting that

$$k_x = k_\rho \cos \alpha_k \ , \qquad k_y = k_\rho \sin \alpha_k \ , \qquad \text{and}$$

$$k'_\rho = k_\rho[\cos \alpha_k \cos \theta + \sin \alpha_k \sin \theta] = k_\rho \cos(\alpha_k - \theta) \quad ,$$

where k_ρ is the magnitude of the component of the wave vector in the antenna spin plane and α_k is the azimuthal angle of the wave vector from the x-axis as shown in Figure 7. The potential measured by the plasma wave instrument will be proportional to the average potential applied across that length of the spacecraft antenna which actively responds to the potential in the plasma. For the moment, assume that the observed potential is the average potential across the antenna lengths from L_1 to L_2. Assuming perfect coupling, the observed potential is given by the following integral:

$$\overline{\phi(t)} = \int_{L_1}^{L_2} \phi(\ell,t)d\ell \Big/ \int_{L1}^{L2} d\ell \tag{8}$$

After integrating Equation 8 and after applying the trigonometric identity $\cos(\alpha) = 1 - 2\sin^2(\alpha/2)$, the observed potential is expressed as the following:

$$\overline{\phi(t)} = \frac{4}{(L_2 - L_1)}(\vec{E}\cdot\hat{\ell})\left(\frac{\sin^2\left(\frac{k'_\rho L_1}{4}\right) - \sin^2\left(\frac{k'_\rho L_2}{4}\right)}{k'^2_\rho}\right)e^{-i\omega t} \quad . \tag{9}$$

The power spectrum (P) observed by the spacecraft is proportional to the square of the measured antenna potential ($\overline{\phi}$), where the antenna potential is purely real for electrostatic waves. The final expression is obtained by time averaging P(t) over the wave period.

$$P \propto \left[(\vec{E}\cdot\hat{\ell})\left(\frac{\sin^2\left(\frac{k'_\rho L_1}{4}\right) - \sin^2\left(\frac{k'_\rho L_2}{4}\right)}{k'^2_\rho (L_2 - L_1)}\right)\right]^2 \tag{10}$$

B. Antenna Coupling to Plasma

Two terms are evident in the above expression. The first term involving $\vec{E}\cdot\hat{\ell}$ is a function of the wave polarization as it projects into the antenna spin plane. This term provides the usual sinusoidal modulation of observed wave intensity as the electric dipole antenna rotates. The second term involving $\sin^2\left(\frac{k'_\rho L}{4}\right)$ is a function of the wave number magnitude and direction and the active lengths of the spacecraft antenna. The ISEE-1 antenna has a tip-to-tip length of 215 meters, of which 143 meters is covered with an insulator. The value of L_2 is 215 meters for ISEE-1 and 30 meters for ISEE-2. For ISEE-2, $L_1 \approx 1$ meter, corresponding to the diameter of the spacecraft body. For ISEE-1, the value of L_1 depends upon whether the antenna responds resistively or capacitively to the applied signal. If the antenna responds resistively, only the uninsulated 36 meters at the ends of the dipole elements contribute to the measured potential. If the antenna responds capacitively, then the entire antenna length contributes to the measured potential. Figure 8 displays the relative amplitude of the second term in Equation 10 as a function of $k_\rho L_2/4$ for $L_1 = 1$ meter and $L_1 = 143$ meters. The value of $k_\rho L_2/4$ is varied from 0 to 3π where $\theta = \alpha_k$. As expected, the log-log plots show a characteristic sin x/x variation with x. For $L_1 = 1$ meter, the amplitude has a power law dependence with wave number, giving a slope of −4. For $L_1 = 143$ meters, however, the amplitude falls off faster than a power law dependence.

To determine the appropriate value of L_1, the critical frequency separating the resistive and capacitive antenna coupling domains must be estimated. Aggson and Kapetanakos [1966] examine the source impedance of a wire antenna as it relates to antenna capacitance. The critical frequency for ISEE-1, in the magnetosheath, will be estimated by computing the ratios of the capacitive and resistive impedances between the Aggson and Kapetanakos study and the present study. In Aggson and Kapetanakos' study a wide range of magnetospheric altitudes were considered. The resistive source impedance (R_s) for a positively charged antenna (due to photo-ionization) is primarily dependent upon particle density and cross-sectional antenna area. Differences in R_s due to density will be removed by choosing an altitude in the Aggson and Kapetanakos study which corresponds to magnetosheath densities. The antenna treated by Aggson and Kapetanakos had a diameter of 1 cm and length of 100 cm. The uninsulated portions of the ISEE-1 antenna have a combined length of 7200 cm and diameter of about 0.1 cm. In Aggson and Kapetanakos' study, the source resistance is very roughly inversely proportional to cross-sectional area. The particle density from Appendix A can be used to select an altitude of 8 R_E, at which the antenna capacitance is computed by Aggson and Kapetanakos to be about 9 $\times 10^{-12}$ farads. Aggson and Kapetanakos computed capacity from the expression

$$C = \frac{2\pi\varepsilon_o d}{\ln\left(\frac{a + \lambda + \sigma\lambda_D}{a}\right)} \tag{11}$$

where d is the antenna length, a is the antenna diameter, λ is the photo-ionization sheath thickness, σ is a constant (≈ 1), and ε_o is the permitivity constant (8.85×10^{-12} farad/m). The photo-ionization sheath thickness λ is computed from the expression

$$\phi_o = \frac{n_e e}{2\varepsilon_o} \left[(a + \lambda)^2 \ln \frac{a + \lambda + \sigma\lambda_D}{a} - \frac{1}{2}[(a + \lambda + \sigma\lambda_D)^2]\right]$$

where ϕ_o is the antenna potential and n_e is the particle density. Assuming an antenna potential on the order of $\phi_o \approx 1$ volt and the electron concentration in Appendix A, the value for λ is found from the above equation to be about 194 cm. Using Equation 11 and this value for

λ, the ISEE-1 antenna capacitance is estimated to be $C \sim 10^{-9}$ farads. The critical frequency is computed based on the following relation

$$f_o \propto \frac{1}{R_s C}$$

and is estimated to be on the order of 3 Hz. The festoon-shaped modulation occurs well above this frequency, and is therefore in the capacitive domain of antenna coupling. It will be assumed that the antenna couples capacitively to the plasma, so that the full length of the dipole elements actively respond to the applied plasma potential ($L_1 = 1$ meter). The left graph in Figure 9, therefore, describes the ISEE-1 antenna response to a spectrum of wave numbers.

C. Model Characteristics

Equation 10 defines the power spectrum of a fine-wire electric dipole antenna's response to a spectrum of wave numbers, as the antenna rotates. Besides antenna length, the antenna response depends primarily upon the angle between the antenna and the electric field and wave vectors projected into the spin plane. The antenna response is illustrated in Figure 9. In this figure, logarithmic, equal-intensity contours are drawn at -5 db, -10 db, -20 db, and -30 db. The vertical axis in the figure is normalized wave number ($k_\rho L_2/4$) and the horizontal axis is antenna rotation angle (θ) in a coordinate system where both the wave vector and polarization electric field vectors are chosen to be at θ = 90 degrees. The normalized wave number is chosen to range from 0 to 3π radians. The basis for choosing this parameter range is that the wave number-angle structure shown in Figure 9 qualitatively reproduces the frequency-time spectral structure of the festoon-shaped events, like that shown in Figure 1. For ISEE-2, the quantity $k_\rho L_2/4$ varies only from 0 to 1.315, for the same variation in k_ρ as plotted for ISEE-1. This means that the festoon-shaped effect will not be seen by the shorter ISEE-2 antenna for the values of k_ρ defined in Figure 9. The festoon-shaped effect will only be seen by ISEE-2, if wavelengths shorter than the antenna length exist in the plasma. For the selected event times, the electron concentration from Appendix A is approximately 58 cm^{-3} and the electron temperature is about 30 eV. This gives a Debye length (λ_{De}) on the order of 5 meters. An order of magnitude measure of the smallest wavelengths which can exist in a plasma is given by $k\lambda_{De} = 1$. The corresponding minimum wavelength is on the order of 34 meters. Because the antenna pattern effect seen in Figure 9 depends upon the existence of wavelengths less than the antenna length of 30 meters, and because wavelengths of this magnitude are not likely to exist, this is an additional reason for not expecting to find the festoon-shaped effect. In fact, no festoon-shaped modulations are found in the ISEE-2 wideband spectrograms.

Based on the above antenna modeling, the existence of wavelengths both shorter and longer than the antenna is sufficient to explain the structure in the frequency-time spectra illustrated in Figure 1. The connection between wave number and frequency is described by the Doppler-shift equation

$$f' = f + \frac{\vec{k}\cdot\vec{V}}{2\pi} \tag{12}$$

where f and $\vec{k}$ are the plasma rest frame frequency and vector wave respectively, $\vec{V}$ is the relative motion of the plasma with respect to the spacecraft, and f' is the spacecraft observed frequency. The spacecraft velocity ~ 2 km/s is much less than the plasma flow velocity, so it will not be included in $\vec{V}$. It will be shown later that the electrostatic waves consist of wavelengths as small as about 36 meters. For plasma flow velocities on the order of 160 km/s, the Doppler shift term may then be as high as 4 kHz. It is clearly possible for a wave of essentially zero frequency (f = 0) in the plasma rest frame to be Doppler shifted into the observed frequency spectrum. For long wavelengths or small wave numbers, only the polarization term in Equation 10 is important. The usual cosine squared variation of intensity with antenna rotation is obtained under this condition. As the wavelength becomes small (on the order of the dipole antenna length and less), the antenna orientation to the wave vector direction becomes important. The minima in intensity satisfy the following relation:

$$m\pi = k_{\rho m}\cos(\alpha_k - \theta)L_2/4 \quad . \tag{13}$$

From this equation, where m is an integer, it is clear that as the antenna angle (θ) becomes perpendicular to $\vec{k}$ (or specifically $\alpha_k - \theta \rightarrow \pm\pi/2$), larger values of $k_{\rho m}$ are required to satisfy the minima condition.

$$k_{\rho m} = \frac{4\pi m}{L_2\cos(\alpha_k - \theta)}$$

The dependence of $k_{\rho m}$ on the antenna rotation angle is the reason for the festoon-shape seen in frequency-time spectra, because the first null in the frequency spectrum is proportional to $k_{\rho m}$, which in turn is proportional to the frequency. This result is similar to the measured power spectrum dependence on wave number and antenna orientation, derived for double-probes by Temerin [1979].

D. Detailed Model Evaluation of Selected Events

The next step is too apply the model described in Figure 9 to a specific event. The objective is to use the antenna response model as a tool for determining the wave mode of the broadband electrostatic emissions. The event selected is on November 22, 1977 (day 326). The event occurs at a time when changes that effect the frequency-time structure, as observed with the wideband receiver, are minimized. The only parameter that must be determined is the orientation angle of the wave vector projected into the antenna spin plane. Figure 5 shows antenna orientations as a function of time and can be used to determine the parameter needed. The vertical time marks at about 37.5 and 39 seconds correspond approximately to the times when the antenna is perpendicular to the wave vector direction, or in this case about 154 degrees and 334 degrees (to the spacecraft-sun line), respectively. By matching the model to these angles and adjusting the vertical registration so as to match the frequency-time shape (in Figure 5) to the wave vector-rotation angle contours (in Figure 9), the antenna response can be adjusted to fit the data. The results of this fitting procedure are shown in Figure 10. Given the limited dynamic range (at best 20db) of the wideband processing film, the antenna response model provides a very good fit to the observed spectrum. The close correspondence between the shape of the model contours and the edge of the visible wideband frequency-time structure is clearly evident in Figure 10. At about 38.95 seconds the sharp "bite-out" at all frequencies corresponds to the point where $\vec{E}\cdot\hat{\ell}$ goes to zero in the antenna response function (see Equation 10). The spectrum at other times follows the model's U-shaped or festoon-shaped appearance. That the bite-out is so sharply defined provides strong evidence that the direction of the projected wave vector distribution must be confined to a line in the antenna spin plane. The bite-out constrains the direction of the projected wave vector (k_ρ) to two possible orientations. The possible orientation angles are 64 degrees and 244 degrees. It is estimated that the wave vector directions must be within ±5 degrees of the above values, otherwise substantial smearing would be observed in the vicinity of the bite-out.

A consequence of fitting the antenna model to the spectrum in Figure 10 is that the frequencies observed in the spacecraft frame of reference are directly and linearly related to the emission wave number component k_ρ. The range of normalized wave number from 0 to 3π

$$0 \leq \frac{k_\rho L_2}{4} \leq 3\pi \tag{14}$$

translates into a range of k_ρ magnitudes given in the following inequality:

$$0 \leq k_\rho \leq 1.75 \times 10^{-3} \text{ cm}^{-1} \tag{15}$$

where L_2 = 215 meters. Because the 10 kHz wideband channel used in Figure 10 has a lower cut-off frequency of 650 Hz and because the 1 kHz channel does not provide clear spectral information, a minimum corresponding to a normalized wave number of 0.853 radians will be used. The ranges of frequency and wave number included in this fitting procedure is expressed in the following inequalities:

$$\begin{aligned} &650 \text{ Hz} \leq f' \leq 2490 \text{ Hz} \\ &1.59 \times 10^{-4} \text{ cm}^{-1} \leq k_\rho \leq 1.75 \times 10^{-3} \text{ cm}^{-1} \end{aligned} \tag{16}$$

where frequency (f') and wave number (k_ρ) are linearly related. It must be noted that the limits defined in Equation 16 do not represent the limits of the observed spectrum, they simply represent corresponding limits for f' and k_ρ. These limits define the range of wave numbers and frequencies to which the antenna response model has been applied. The range of the wave number magnitude given in Equation 16 also translates into a range of wavelengths in terms of the Debye length given in the previous section

$$7\lambda_{De} \leq \lambda \leq 74\lambda_{De} \quad .$$

The observed frequency and total wave number ($\vec{k}$, $|\vec{k}|^2 = {k_\rho}^2 + {k_z}^2$) are also related by the Doppler-shift given by Equation 12, where k_z is the z-component of the wave vector.

Because nothing is specifically known about the magnitude of k_z, the limits in Equation 16 provide constraints in wave number-frequency space for the waves observed. The allowed regions of wave-number and frequency are obtained by varying k_z from negative infinity to positive infinity, for the two allowed orientation angles of k_ρ, to compute the corresponding values of frequency (f). This is done by expressing the Doppler shift equation as a function of f.

$$f = f' - \frac{1}{2\pi}\left(k_\rho(V_x \cos \alpha_k + V_y \sin \alpha_k) + k_z V_z\right) \tag{17}$$

The linear relation between the observed frequency (f') and wave number (k_ρ) can be expressed as

$$f' = ak_\rho + b \tag{18}$$

where the fit in Figure 10 gives $a=1.16 \times 10^6$ cm.s^{-1} and b=466 Hz. Using the expression for f' in Equation 18 in Equation 17, the following expression is obtained:

$$f = \frac{(a - V_x \cos \alpha_k + V_y \sin \alpha_k)k_\rho}{2\pi} + b - \frac{V_z k_z}{2\pi} \tag{19}$$

For the two possible values of α_k (64 degrees and 244 degrees), for k_z varying from $-\infty$ to $+\infty$ at fixed values of k_ρ, and for selected values of k_ρ at 1.59×10^{-4} cm^{-1}, 3.5×10^{-4} cm^{-1}, 7.8×10^{-4} cm^{-1}, and 1.74×10^{-3} cm^{-1}, curves of allowed wave number-frequency values are shown in Figure 11. Two curves are obtained for each value of k_ρ. The curve corresponding to $\alpha_k = 64°$ minimizes higher in frequency than the other curve and exists for both positive and negative k_z. Solutions do not exist for α_k=244 degrees and k_z>0. These four families of curves are representative of a spectrum of possible wave number-frequency values for k_ρ varying smoothly over the range defined in Equation 16. The shaded region in Figure 11 defines those values which are allowed. Those values are approximately limited at large wave number by $k\lambda_{De} \leq 1$ ($T_e \approx$ 30 eV). The more lightly shaded regions define values allowed by only one of the two possible k_ρ orientations. The more heavily shaded region defines wave number and frequency values allowed with either orientation of k_ρ. The curve defining equal phase ($V_p = \omega/k$) and electron thermal velocities (V_{Te}) is also included in the illustration. Because cold plasma theory is only valid for $V_{Te}/V_p << 1$, warm or hot plasma theory will be necessary for describing the observed emissions.

IV. IDENTIFICATION OF PLASMA WAVE MODES

The previous section developed an antenna response model which leads to constraints on the possible values of wave number and frequency for a particular event. It is the objective of this section to examine the commonly known plasma wave modes as they relate to the plasma environment in order to try to identify the wave modes involved in producing the festoon-shaped features. Those wave modes which may contribute to the emissions are determined by means of this examination. Appendix A lists measured and computed plasma parameters which will be useful in the following analysis.

A. Cold Plasma Modes

Although Figure 11 indicates that cold plasma descriptions are not valid, at least for electron wave modes, cold plasma formalism provides useful descriptions of most of the wave modes found in hot plasma theories. The treatment of Stix [1962] will be followe. for a review of cold plasma wave theory.

Beginning at the lowest frequencies are the hydromagnetic wave modes or Alfven waves. The corresponding dispersion curves are shown in Figure 12 for frequencies below 10^{-2} Hz. The shaded regions shown in this illustration represent the track of the solutions of the cold plasma dispersion as the angle of the wave vector to the magnetic field is varied from 0 degrees to 90 degrees. The region corresponding to the slow-mode Alfven wave is shown for angles only to 75 degrees. This mode disappears as θ approaches 90 degrees. Both Alfven wave modes are electromagnetic, except at very low frequencies and at certain angles. It is clear from the dispersion curves in Figure 12, that the corresponding wave numbers are too small to contribute to the festoon-shaped electrostatic emissions.

The slow-mode Alfven wave becomes the ion cyclotron wave as $\omega \to \omega_{ci}$. For a two component plasma there is a resonance at the ion cyclotron frequency for $\theta = 0$ degrees which moves to lower frequencies as θ becomes larger. The mode disappears as $\theta \to 90$ degrees, just as the slow-mode Alfven modes disappear. Although the resonant dispersion curve intersects the region of wave number-frequency space required for festoon-shaped emissions, ion cyclotron waves do not exist in a thermal plasma at wavelengths much less than the ion gyroradius [Stix, 1962]. From the magnetic field strength in Appendix A and an ion temperature of about 90 eV (see Figure 1 of Sckopke et al. [1981], the ion gyroradius is about 40 km. The festoon-shaped events have wavelengths much less than this, therefore, ion cyclotron waves can be excluded from further consideration.

The fast-mode Alfven wave dispersion relation is unaffected by the ion cyclotron frequency, but encounters a resonance which moves from the electron cyclotron frequency to the lower hybrid resonance as θ varies from 0 degrees to 90 degrees, respectively. The wave modes which have resonance angles between the electron cyclotron frequency and lower hybrid resonance are called whistler mode waves. There is also a resonance at the upper hybrid frequency. This latter resonance, however, is not apparent in Figure 12 due to the proximity of a cutoff for this mode (at $L = 0$) to resonance at the electron plasma frequency. Both of these modes are also electromagnetic, except at resonance where the modes become quasi-electrostatic. Although resonance at the upper hybrid frequency may reach large wave numbers, this mode is too high in frequency to account for the festoon-shaped spectrograms. Above the electron plasma frequency, the quasi-longitudinal wave mode is electromagnetic and also too high in frequency to account for the festoon-shaped spectrograms.

Whistler mode resonances remain a possible source of the festoon-shaped events. Additional constraints on whistler mode waves may be derived, because of the characteristics of a wave mode at a resonance. Before proceeding, it is desirable to sketch the geometry in the antenna spin-plane, as is done in Figure 13. The projected plasma flow and magnetic field vectors are shown along with the orientation of k_ρ. Because k_ρ is confined to a line in the antenna spin-plane and k_z is essentially unknown, there exists a plane within which the wave vector must be contained. For this special case, that plane can be projected into a line in the spin-plane. Additional restrictions can be made by realizing that resonance of a whistler wave mode at a particular angle to the magnetic field is a source of large wave numbers. A wave vector directed along a resonance cone could produce the required wave number spectrum, but would be characterized by wave vectors confined to a narrow range of angles to the magnetic field. From the resonance cone angle (α_{kB}), it is possible to solve for k_z from the following equation

$$\vec{k}\cdot\vec{B} = kB\cos\alpha_{kB} = k_\rho(B_x\cos\alpha_k + B_y\sin\alpha_k) + k_zB_z \qquad (20)$$

where $k = \sqrt{k_\rho^2 + k_z^2}$.

Equation 20 is quadratic in k_z and for each of the two possible values of α_k, two values of k_z can be computed. The roots of Equation 20 are plotted in Figure 14. As might be expected, the roots are double valued along the two curves which are plotted. Naturally, the values of the solutions for k_z or equivalently for $|\vec{k}|$ depend upon the value of k_ρ. Equation 16 defines the range of k_ρ which is known to exist. If the maximum value for k_ρ from Equation 16 is used, the largest $|\vec{k}|$ which would be known to exist for a given resonance cone angle could be found. It is for these values that the curves in Figure 14 are plotted. This means that a given resonance cone angle requires the existence of wave numbers at least as large as those defined by the curves in Figure 14. Krall and Trivelpiece [1973] determined that for a Maxwellian particle velocity distribution, whistler mode waves are weakly Landau damped except for wavelengths less than the electron cyclotron radius, $\lambda \lesssim a_{ce}$, where

$$a_{ce}^2 = \frac{kT_e}{m_e\omega_{ce}^2} = \lambda_{De}^2\frac{\omega_{pe}^2}{\omega_{ce}^2}$$

From the parameters in Appendix A, the condition for strong damping becomes $\lambda \lesssim 100\ \lambda_{De}$. Because whistler mode waves will be strongly damped for the wave numbers known to exist, it is unlikely that the whistler mode is responsible for the festoon-shaped events.

The remaining cold plasma wave modes occur at high frequencies just above the electron plasma frequency. These are quasi-transverse "ordinary" and "extraordinary" waves. They exhibit a cutoff at and just above the electron plasma frequency. Both waves are electromagnetic and can be discarded as candidates for explaining the magnetosheath electrostatic emissions.

B. Hot Plasma Modes

There are several electrostatic wave modes which are unique to hot plasma theory. The first to be considered are the solutions of the Harris dispersion equation at $\theta = \pi/2$, called Bernstein modes. Bernstein modes are solutions to the Harris dispersion relation at frequencies between either the ion or the electron cyclotron harmonics. The condition for the instability of Bernstein mode waves is that $\partial f_o/\partial v_\perp > 0$ for some range of $v_\perp > 0$ [Tantaronis and Crawford, 1970]. Electron and proton particle distribution functions at energies from 215 eV to 45 keV as measured by the quadrispherical LEPEDEA on board ISEE-1 are characteristic of near subsolar magnetosheath flows at the event times chosen for study [T. E. Eastman, private communication, 1982]. There is no positive slope in these particle velocity distribution functions. That no positive slope in the plasma particle distribution function is found is not conclusive evidence that it does not exist, since a positive slope to the distribution function may exist at lower energies. However, it is likely that such a distribution is not a common feature of the magnetosheath [T. E. Eastman, private communication, 1982]. For the ion and electron temperatures stated in the previous section, the electron and proton cyclotron radii are 540m and 40km, respectively. Because these cyclotron radii are the characteristic length scales of the Bernstein modes, and because the wavelengths of the electrostatic waves in the magnetosheath are much less than these cyclotron radii, it is unlikely that the Bernstein modes are associated with these waves.

Besides low frequency-long wavelength particle drift or gradient wave modes, the only wave mode remaining to be considered is the ion acoustic mode. For the conditions $\omega_{ci} \ll \omega_{pi}$ and $\omega \gg \omega_{ci}$, which are valid in the regime being considered, descriptions of the ion-acoustic mode may be approximated by the case for zero magnetic field. Krall and Trivelpiece [1973] derive a dispersion equation for ion acoustic waves from linearized Vlasov theory of plasma waves in the free field case and using a Maxwellian distribution function.

$$\omega_{REAL}^2 = \frac{k^2 C_s^2}{1 + k^2 \lambda_{De}^2} \tag{21}$$

These waves are called sound waves because for $k\lambda_{De} \ll 1$ all wavelengths propagate at the ion sound speed C_s. For a Maxwellian velocity distribution, the only condition given for the weak damping of these waves is that $T_e \gg T_i$. Stated another way, the ion and electron thermal velocities must be related to the phase velocity as shown in the following inequality:

$$\left(\frac{kT_i}{m}\right)^{1/2} < \frac{\omega}{k} < \left(\frac{kT_e}{m_e}\right)^{1/2} \qquad (22)$$

Equation 21 is plotted in Figure 15, against the region of antenna model constrained wave number and frequency. The dispersion curve intersects the shaded region from about 150 Hz to 1 kHz. Ion-acoustic mode wave emission within this frequency range will satisfy observationally imposed constraints. Note that this does not require wave emission at all frequencies within the range, only some frequencies within the range. For a plasma flow of 156 km/s (from Appendix A) and for a maximum wave number of about 1.8×10^{-3} cm^{-1} (from Figure 15), Doppler shifts may be as large as $kV/2\pi$ = 4500 Hz (from Equation 12). Depending upon the angle between the wave number and plasma flow velocity, the observed emission spectrum can be produced. Figure 15 also appears to resolve the ambiguity in the orientation of k_ρ. For $\alpha_k = 244°$, the full rest-frame spectrum limits marked in Figure 15 are allowed. The spectrum for $\alpha_k = 64°$ is limited to frequencies no less than about 500 Hz. Also, if $k\lambda_{De} = 1$ is used to roughly indicate the level of Landau damping, then damping will be less for $\alpha_k = 244°$ than for $\alpha_k = 64°$. The addition of a magnetic field into a description of the ion-acoustic mode can also result in the resonant frequency rising to about $\sqrt{1.6}\omega_{pi}$ [Stix, 1962]. For such a situation, higher values of k_ρ may be reached without increasing the total wave number. The orientation of k_ρ for $\alpha_k = 244°$ will still result in less damping than for $\alpha_k = 64°$. It is therefore, more likely that the vector wave numbers are aligned with $\alpha_k = 244°$. This orientation is generally downstream of the bow shock in the direction of the bulk plasma flow.

VI. DISCUSSION

Some early electric field wave observations of the magnetosheath were made with the IMP-6 spacecraft [Rodriguez and Gurnett, 1975; Rodriguez, 1979]. These studies found electrostatic waves polarized generally along the magnetic field, with frequency spectra similar to that found in the present study. Rodriguez [1979] concluded that the emissions below the ion plasma frequency were likely to be ion-acoustic waves, with wavelengths longer than 100 meters. Rodriguez and Gurnett [1975] found parabola-shaped bursts below 1 kHz. The basic differences between the instrumentations used in these studies and the present study are the antenna lengths and spacecraft rotation rates. The ISEE-1 215 meter antenna is more than twice the length of the longest IMP-6 antenna (93.2 meters) and the ISEE-1 spin period of 3 seconds is much less than the 11.1 second IMP-6 spin period. The parabola-shaped bursts are probably due to an antenna effect.

Emissions likely to be ion-acoustic mode waves have been found upstream of the bow shock (foreshock) in the solar wind [Anderson et al., 1981]. Although no festoon-shaped effect was reported, Figure 14 of Anderson et al. [1981] shows evidence of a rising and falling emission band with periods on the order of half the spacecraft rotation period. It is possible that this is also an antenna pattern effect. Outward flowing particles apparently reflected at the bow shock and associated with ion-acoustic mode waves in the Earth's foreshock are also observed [Eastman et al., 1981]. More recently, unstable electron particle distributions have been found just inside the Earth's bow shock [Feldman et al, 1982]. The distributions are characterized by a convecting Maxwellian superimposed on a Lorentzian distribution. This particle distribution is found to be a common characteristic of the plasma just inside the bow shock. The distribution is believed to be unstable to ion-acoustic waves in the frequency range from 100 Hz to 1.5 ω_{pi} [private communication, M. F. Thomsen, 1982], although correlations with wave observations have not yet been done.

The generation of ion-acoustic mode waves could occur at locations within the outer magnetosheath or at a surface such as the bow shock. It has been stated that the festoon-shaped spectrograms, which probably result from ion-acoustic mode waves, are seen at widely ranging locations in the outer magnetosheath, and at the bow shock. The gradually decreasing intensity of these waves as one proceeds into the magnetosheath from the shock provides strong evidence that the waves are generated at the bow shock and convected downstream into the magnetosheath. Generation of the emissions at the bow shock is supported because particle distributions unstable to ion-acoustic waves have not been commonly found within the magnetosheath [T. E. Eastman, private communication, 1982]. Particle distributions that may be unstable to the ion-acoustic mode have been found at the bow shock [Feldman et al., 1982]. Examination of the ion-acoustic mode group velocities ($V_g = \partial\omega/\partial k$) for the frequency range of interest finds the magnitudes to be less than the plasma flow velocity. From about 150 Hz to 1 kHz the ion-acoustic mode group velocity is at least a factor of 3 less than the plasma flow velocity, so these waves will be carried by the bulk plasma flow. If the nominal magnetosheath plasma is not unstable to ion-acoustic waves, the emissions must originate in association with the bow shock and be convected to spacecraft locations within the outer magnetosheath. Because the group velocity is much less than the plasma flow velocity generation at the magnetopause or in the magnetosphere is not likely.

Further evidence for bow shock generation of the festoon-shaped events comes from the observed wave vector geometry. Wave vectors projected into the spin-plane are found to lie within a narrow range of angles at any given moment. The orientation of the projected wave vectors has no apparent relation to the local magnetic field or plasma flow velocity. Therefore, there is no apparent local reason for the wave vector orientation. Should wave vectors be produced at orientations defined by the bow shock surface, that orientation might be preserved as the wave is convected downstream. Variation in the local orientation of the plane containing the wave vector would then reflect a time history of the variation of the surface of the bow shock immediately upstream of the spacecraft. A systematic drop in the intensity of the festoon-shaped events with distance from the bow shock (into the magnetosheath) provides additional confirming evidence. The variation in intensity as a function of the distance from the bow shock can be seen in Figure 4 for those frequency channels covering the ion-acoustic wave spectrum. These logarithmically displayed intensities are a maximum just inside the bow-shock and decline in intensity until the festoon-shaped events disappear near 1000 UT. At 600 Hz, the spectral power flux decreases at a rate of about 3db per 100 km for the first 2000 km after the bow shock and remains fairly constant until about 1000 UT. This effect is consistent with waves which are produced at the bow shock and dissipate as they are convected away from the source of free energy driving the instability.

A concern associated with the propagation of ion-acoustic waves from the bow shock to spacecraft locations within the magnetosheath is that ion-acoustic waves are strongly damped unless $T_e/T_i << 1$. Thorne and Tsurutani [1981] state that magnetosheath protons have thermal energies considerably larger than electrons ($T_i \approx 200$ eV and $T_e \approx 30$ eV). In general, the ion to electron temperature ratio in the magnetosheath is found to be $3 \leq T_i/T_e \leq 10$ [Ogilvie and Scudder, 1979; Sckopke et al., 1981; T. E. Eastman, private communication, 1982]. For the specific event studied, and the measured plasma flow and wave group velocities, the transit time of ion-acoustic waves from the bow shock to the spacecraft is no less than about 30 seconds. If the ion-acoustic waves were heavily damped by the magnetosheath plasma, they would not be observed at the spacecraft location. As discussed above, some damping is evident as the spacecraft becomes further from the bow shock. However, detailed growth rate calculations with observed particle distributions are necessary, before it can be determined if bow shock wave generation is consistent with these observations. Of interest is the appearance of two levels of damping in Figure 6. The effect may reflect the thermalization of solar wind ions entering the magnetosheath. Electrons experience an abrupt change in thermal temperature at the bow shock, while ions thermalize more slowly [M. F. Thomsen, private communication, 1982]. Because the damping of ion-acoustic waves will be strongly influenced by T_e/T_i, the sharp drop in intensity of the waves during the first 2000 km after crossing the bow shock and passing into the magnetosheath may correspond to the region over which solar wind ions thermalize in the magnetosheath and at the bow shock.

VI. CONCLUSIONS

This study has sought to explore the characteristics and causes of the "festoon-shaped" electric field spectrum found in the Earth's magnetosheath. The importance of understanding these emissions is evident by their frequent occurrence. They are seen over wide ranges of local time and across the outer magnetosheath. The "festoon-shape" seen in frequency-time spectrograms results from the antenna pattern for electric field wavelengths comparable to the ISEE-1 antenna length (L = 215 meters). Given the Doppler shift of a plasma frame spectrum of wave numbers, the observed frequency is shown to be linearly related to the wave vector component in the antenna spin-plane. The fine time structure evident in the spectral shape is a consequence of the narrow confinement of all wave number vectors to a plane which contains the z-axis in GSE coordinates and projects to a line in the antenna spin plane.

Of all the cold and hot plasma wave modes considered, the restrictions which are imposed upon possible wave number-frequency values in the plasma frame of reference eliminate likely participation of all but one normal plasma wave mode in the generation of these emissions. That mode is the ion-acoustic wave mode.

In the rest frame of the plasma, the ion-acoustic waves are produced at frequencies in the range from about 150 Hz to 4 kHz and at wavelengths from about 30 meters to 600 meters. The ion-acoustic waves are thought to be produced upstream at the Earth's bow shock, where electrons passing through a shock acceleration region produce an unstable particle velocity distribution. It is additionally hypothesized that the wave vectors are produced with orientations defined by the bow shock surface and that this geometry is characteristic of the waves as they are convected into the magnetosheath. The festoon-shaped events and, therefore, ion-acoustic waves are found to be a common characteristic of the Earth's dayside magnetosheath.

A self-consistent picture has been assembled of the magnetosheath environment during the observation of electrostatic fields which exhibit a "festoon-shaped" frequency-time structure in phase with the rotation of the observing dipole antenna. This does not mean that these observations may have no other explanation. It does mean that any explanation of all salient features is highly constrained by the collection of presented evidence. Should this picture be sustained by subsequent investigation, an additional tool is obtained for the study of the complex processes operating in the Earth's magnetosheath and at the bow-shock.

ACKNOWLEDGEMENTS

The author wishes to thank D. A. Gurnett for his valuable assistance in the preparation of this work. This work was supported by the National Aeronautics and Space Administration through Contracts NAS5-20093 and NAS5-26819 with Goddard Space Flight Center, Grants NGL-16-001-002 and NGL-16-001-043 with NASA Headquarters, and the Office of Naval Research.

REFERENCES

Aggson, T.L., and C.A. Kapetanakos, On the impedance of a satellite borne VLF electric field antenna, NASA, X-612-66-380, 1966.

Anderson, R.R., C.C. Harvey, M.M. Hoppe, B.T. Tsurutani, T.E. Eastman, and J. Etcheto, Plasma waves near the magnetopause, J. Geophys. Res., 87, 2087-2107, 1982.

Anderson, R.R., G.K. Parks, T.E. Eastman, D.A. Gurnett, and L.A. Frank, Plasma waves associated with energetic particles streaming into the solar wind from the Earth's bow shock, J. Geophys. Res., 86, 4493-4510, 1981.

Eastman, T.E., R.R. Anderson, L.A. Frank, and G.K. Parks, Upstream particles observed in the Earth's foreshock region, J. Geophys. Res., 86, 4379-4395, 1981.

Feldman, W.C., R.C. Anderson, S.J. Bame, S.P. Gary, J.T. Gosling, D.J. McComas, M.F. Thomsen, G. Paschmann, and M.M. Hoppe, Electron velocity distributions near the Earth's bow shock, submitted for publication to J. Geophys. Res., 1982.

Frank, L.A., K.L. Ackerson, R.J. DeCoster, and B.G. Burek, Three-dimensional plasma measurements within the Earth's magnetosphere, Space Sci. Rev., 22, 739-763, 1978.

Frank, L.A., D.M. Yeager, H.D. Owens, K.L. Ackerson, and M.R. English, Quadrispherical LEPEDEAS for ISEE-1 and -2 plasma measurements, IEEE Trans. Geosci. Electr., GE-16, 3, 221-224, 1978.

Gurnett, Donald A., and Robert R. Shaw, Electromagnetic Radiation trapped in the magnetosphere above the plasma frequency, J. Geophys. Res., 78, 8136-8149, 1973.

Gurnett, D.A. and L.A. Frank, and R.P. Lepping, Plasma waves in the distant magnetotail, J. Geophys. Res., 81, 6059-6071, 1976.

Gurnett, D.A. and L.A. Frank, A region of intense plasma wave turbulence on auroral field lines, J. Geophys. Res., 82, 1031-1050, 1977.

Gurnett, D.A., F.L. Scarf, R.W. Fredricks, and E.J. Smith, The ISEE-1 and ISEE-2 plasma wave investigation, IEEE Trans. Geosci. Electr., GE-16, 3, 225-230, 1978.

Kintner, P.M. Jr., Observations of velocity shear driven plasma turbulence, J. Geophys. Res., 81, 5114-5122, 1976.

Krall, Nicholas A., and Alvin W. Trivelpiece, Principles of Plasma Physics, McGraw-Hill, 1973.

Kraus, John D., Radio Astronomy, McGraw-Hill, 1966.

Ogilvie, K.W. and M.D. Banks, Jr., Notes on the ISEE A+B data pool tape, NASA/Goddard Space Flight Center, X-692-77-129, 1977.

Ogilvie, K.W., and J.D. Scudder, First results from the 6-axis electron spectrometer on ISEE-1, Space Sci. Rev., 23, 123-133, 1979.

Rodriguez, Paul, Magnetosheath electrostatic turbulence, J. Geophys. Res., 84, 917-930, 1979.

Rodriguez, Paul and Donald A. Gurnett, Electrostatic and electromagnetic turbulence associated with the Earth's bow shock, J. Geophys. Res., 80, 19-31, 1975.

Sckopke, N., G. Paschmann, G. Haerendel, B.U.O. Sonnerup, S.J. Bame, T.G. Forbes, E.W. Hones, and C.T. Russell, Structure of the low-latitude boundary layer, J. Geophys. Res., 86, 1981.

Stix, Thomas Howard, The Theory of Plasma Waves, McGraw-Hill, 1962.

Tantaronis, J.A., and F.W. Crawford, Cyclotron harmonic wave propagation and instabilities, I. Perpendicular propagation, J. Plasma Phys., 4, 231-248, 1970.

Temerin, Michael, Dopler shift effects on double-probe-measured electric field power spectra, J. Geophys. Res., 84, 5929-5934, 1979.

Thorne, R.M., and B.T. Tsurutani, The generation mechanism for magnetosheath lion roars, Nature, 293, 384-386, 1981.

Tsurutani, B.T., E.J. Smith, R.R. Anderson, K. W. Ogilvie, J.D. Scudder, D.N. Baker, and S.J. Bame, Lion roars and non-oscillatory drift mirror waves in the magnetosphere, submitted to J. Geophys. Res., 1982.

APPENDIX A:

MEASURED AND COMPUTED PLASMA PARAMETERS

Basic Plasma and Wave Environments

density $n = n_e = n_i = 58\ cm^{-3}$

[Bame experiment, Ogilvie and Banks, 1977; verified with plasma wave data]

magnetic field $|\vec{B}_o| = 24.4$ nT, $B_{ox} = 5.91$ nT, $B_{oy} = 20.4$ nT, $B_{oz} = 11.9$ nT
[Russell experiment, Ogilvie and Banks, 1977]

kinetic electron temperature $T_e = 30$ eV
[Tsurutani, 1982]

plasma flow velocity $|\vec{V}| = 156$ km/s, $V_x = -113$ km/s, $V_g = -74$ km/s, $V_z = 78$ km/s
[T. E. Eastman, private communication, 1982]

thermal electron energy density $U_T = nkT = 2.8 \times 10^{-9}\ erg/cm^3$

maximum average electric field energy density $U_E = \frac{E^2}{8\pi} = 4.9 \times 10^{-22}\ erg/cm^3$

Computed Plasma Parameters and Frequencies

Thermal/magnetic energy ratio	$\beta = 1.2$
Thermal electron velocity	$V_{Te} = 2.3 \times 10^8$ cm/s
Electron Debye length	$\lambda_{De} = 530$ cm
Ion sound speed	$C_s = 5.4 \times 10^6$ cm/s
Electron plasma frequency	$f_{pe} = 68$ kHz $\equiv \omega_{pe}/2\pi$
Electron gyrofrequency	$f_{ce} = 680$ Hz $\equiv \omega_{ce}/2\pi$
Ion plasma frequency (H^+)	$f_{pi} = 1.6$ kHz $\equiv \omega_{pi}/2\pi$
Ion gyrofrequency (H^+)	$f_{ci} = 0.37$ Hz $\equiv \omega_{ci}/2\pi$
Upper hybrid resonance	$f_{UHR} = 68$ kHz $\equiv \omega_{UHR}/2\pi$
Lower hybrid resonance	$f_{LHR} = 16$ Hz $\equiv \omega_{LHR}/2\pi$
Electron plasma to gyrofrequency ratio	$\omega_{pe}/\omega_{ce} = 100$

FIGURE CAPTIONS

Figure 1 Wideband data from the ISEE-1 spacecraft on December 20, 1977 (day 354) illustrate the characteristic festoon-shaped emissions found in the Earth's dayside magnetosheath. The spacecraft is located at about 18.6 R_E, 13.1° magnetic latitude, and 7.45 hours magnetic local time. The lower panel shows an electric field spectrogram for the frequency range of 0 to 5 kHz and for times from 18h 42m 28s to 18h 42m 54s universal time (higher intensities are shown as darker shading). The upper panel shows the trace of the upper frequency cutoff of the emission as a function of time. The rise and fall of the cutoff is directly related to the rotation of the spacecraft's dipole antenna.

Figure 2 Wideband data from ISEE-1 is shown for November 22, 1977 (day 326) from 9h 57m 0s to 9h 57m 15s. The spacecraft is located at about 12.4 R_E, 12.9° magnetic latitude, and 10.9 hours magnetic local time. Both panels display frequency-time spectrograms; the upper panel from 0 to 10 kHz and the lower panel from 0 to 1 kHz. The 10 kHz channel has a low frequency instrument cutoff at 650 Hz and data below 150 Hz in the 1kHz channel has been eliminated in order to enhance the shading of the higher frequencies. In the interval from 6 seconds to 9 seconds, the festoon-shaped emission bandwidth varies from 200 Hz-800 Hz at about 6.5 seconds to 400 Hz - 2 kHz at about 7.5 seconds.

Figure 3 In panel (a), wideband data from ISEE-1 is shown for November 22, 1977, (day 324) from 9h 57m 15s to 9h 57m 30s. The spacecraft is located at about 12.4 R_E, 12.9° magnetic latitude, and 10.9 hours magnetic local time. A second frequency component is evident at about 23 seconds, however, it may be unrelated to the main emission spectrum. In panel (b), wideband data from ISEE-1 is shown from 9h 59m 30s to 9h 59m 45s. The frequency-time structure rises as high as 6 kHz, showing gaps in intensity near 37 seconds and 39 seconds. The 10 kHz channel in both panels has a low frequency instrument cutoff at 650 Hz.

Figure 4 Spectrum analyzer data for November 22, 1977 are shown for the electric field antenna. The spectrum analyzer channels are displayed vertically with frequency increasing upward. Time increases to the right. The electric field spectral intensity in each channel is displayed logarithmically.

Spacecraft coordinates are shown at the bottom of the panel in geocentric magnetospheric coordinates. Bow shock and magnetopause are marked to delineate the passage of the spacecraft through the magnetosheath, where the festoon-shaped events are studied. The arrow indicates the event time modeled in Figure 10.

Figure 5 The event time shown in Figure 3(b) is expanded in frequency and displayed along with the orientation of the spacecraft antenna with respect to the spacecraft-sun line, the magnetic field, and the plasma flow velocity. Vertical reference lines are drawn to determine the antenna orientation when the emission bandwidth is a maximum. For those marked times, the average antenna to magnetic field and plasma flow velocity angles are 77 ±4 degrees and -60 ±6 degrees, respectively.

Figure 6 ISEE-1 antenna orientation to the magnetic field and plasma flow velocities are summarized for 15 event times like those times marked with vertical lines in Figure 5. Orientation angle is found to be reasonably constant over time intervals of 6 seconds to 10 seconds, however, not coherent over time intervals of 140 seconds or longer.

Figure 7 Electric field and wave vectors are shown along with angle definitions. These definitions are those used in developing the antenna response to a spectrum of wave numbers. The antenna spin-plane component of $\vec{k}$ is k_ρ and and its azimuthal angle to the GSE coordinate x-axis is α_k. The vector $\vec{\ell}$ is along the electric dipole antenna and θ defines its azimuthal orientation.

Figure 8 Relative antenna response intensity, for antenna orientation along the polarization electric field, as a function of wave number and for two parameter conditions are shown. For L_1=1 meter, the intensity is power law with spectral index of -4 at wavelengths less than the antenna length. For L_1=143 meters the fall-off in intensity is more rapid than power law. The smaller value is appropriate for capacitive antenna coupling to the plasma and the larger value, for resistive coupling. For magnetosheath conditions, the antenna couples capacitively to the plasma (L_1 = 1 meter).

Figure 9 Antenna model response to a spectrum of wave numbers is summarized. Contours trace equal intensity levels at labeled decibel values referenced to the peak value. The model qualitatively reproduces the emission festoon-shape and the intensity gap at all frequencies for antenna orientations perpendicular to the polarization electric field. The wave number and electric field vectors are both at $\theta = 90°$ for the purpose of illustrating the antenna response to a spectrum of wave numbers.

Figure 10 Antenna response intensity contours are compared directly to an event observed with the wideband receiver. The left vertical axis is the normalized wave number (just as in Figure 9), the bottom horizontal axis is the event time, the right vertical axis is the frequency scale corresponding to the wideband data displayed, and the top horizontal axis is the antenna orientation angle to the spacecraft-sun line for both the model and data during this event. The contour lines are found to reproduce the festoon-shape spectrum and also reflect the shape of the intensity gap at about 38.95 seconds. The intensity dropout is about 5 degrees wide in spacecraft rotation at 1.3 kHz and widens to 15 degrees at about 2 kHz.

Figure 11 The values of wave number and frequency which are allowed for selected magnitudes of the spin-plane projected wave number (k_ρ) are plotted. For each value of k_ρ, two curves result. As shown in the inset, one curve corresponds to k_ρ chosen to lie in the dusk half plane of the GSE X-Y plane (α_k = 64 degrees) and the other corresponds to k_ρ in the dawn half plane (α_k = 244°). The curve is formed by varying k_z from $-\infty$ to $+\infty$ and computing total wave number and frequency from Equation 19. For k_ρ in the dawn half plane, there are no solutions for $k_z>0$. Four families of curves are plotted corresponding to values of k_ρ which cover the modeled range 1.59×10^{-4} cm^{-1}, 3.5×10^{-4} cm^{-1}, 7.8×10^{-4} cm^{-1}, and 1.75×10^{-3} cm^{-1}. The more lightly shaded regions correspond to wave number and frequency values which can only be reached by one of the α_k values. The more darkly shaded region is accessible for α_k equal to 64° or 244°.

Figure 12 All cold plasma wave mode dispersion curves are shown for the plasma parameters defined in Appendix A. Wave number angles to the magnetic field from 0° to 90° sweep out regions which are shaded to reflect the sense of polarization for electromagnetic waves. Quasi-linear polarization is shown as a solid line.

Figure 13 The spin-plane geometry corresponding to the modeled event in Figure 10 is shown. The projected plane which must contain the wave vectors is at an angle of 64 degrees to the sun direction in the GSE X-Y plane. The projected plasma and magnetic field vectors are also shown.

Figure 14 The whistler wave mode satisfies the required wave number spectrum (k_ρ) only at a resonance cone. The roots of the solutions for the largest wave numbers consequently known to exist are plotted. Resonance cone angles which require $|\vec{k}|$ to be very near or larger than the electron gyroradius ($k\lambda_{De} \approx 2\pi/100$) will be strongly damped.

Figure 15 The ion-acoustic mode dispersion equation is plotted against the allowed values of wave number and frequency from Figure 11. Before resonance at the ion plasma frequency, the dispersion curve crosses allowed wave numbers from about 150 Hz to 1 kHz. For plasma flow relative to the spacecraft of about 156 km/s and maximum wave number of 1.8×10^{-3} cm^{-1}, Doppler shifts as large as 4500 Hz are possible. The spacecraft observed frequency spectrum can be produced by the ion-acoustic wave mode.

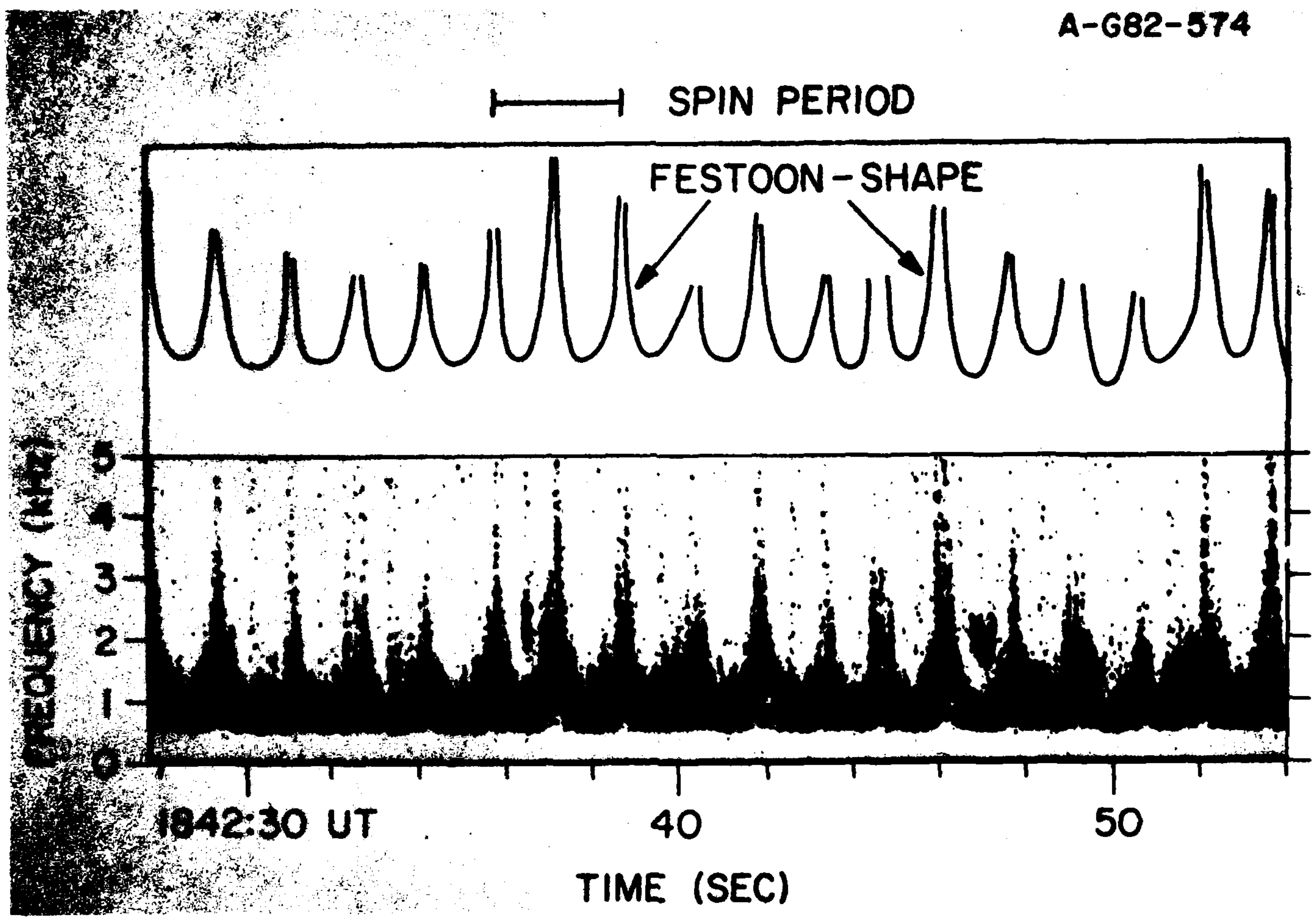
A-G82-574
SPIN PERIOD
FESTOON-SHAPE
FREQUENCY (kHz)
0
1
2
3
4
5
1842:30 UT
40
50
TIME (SEC)

Figure 1

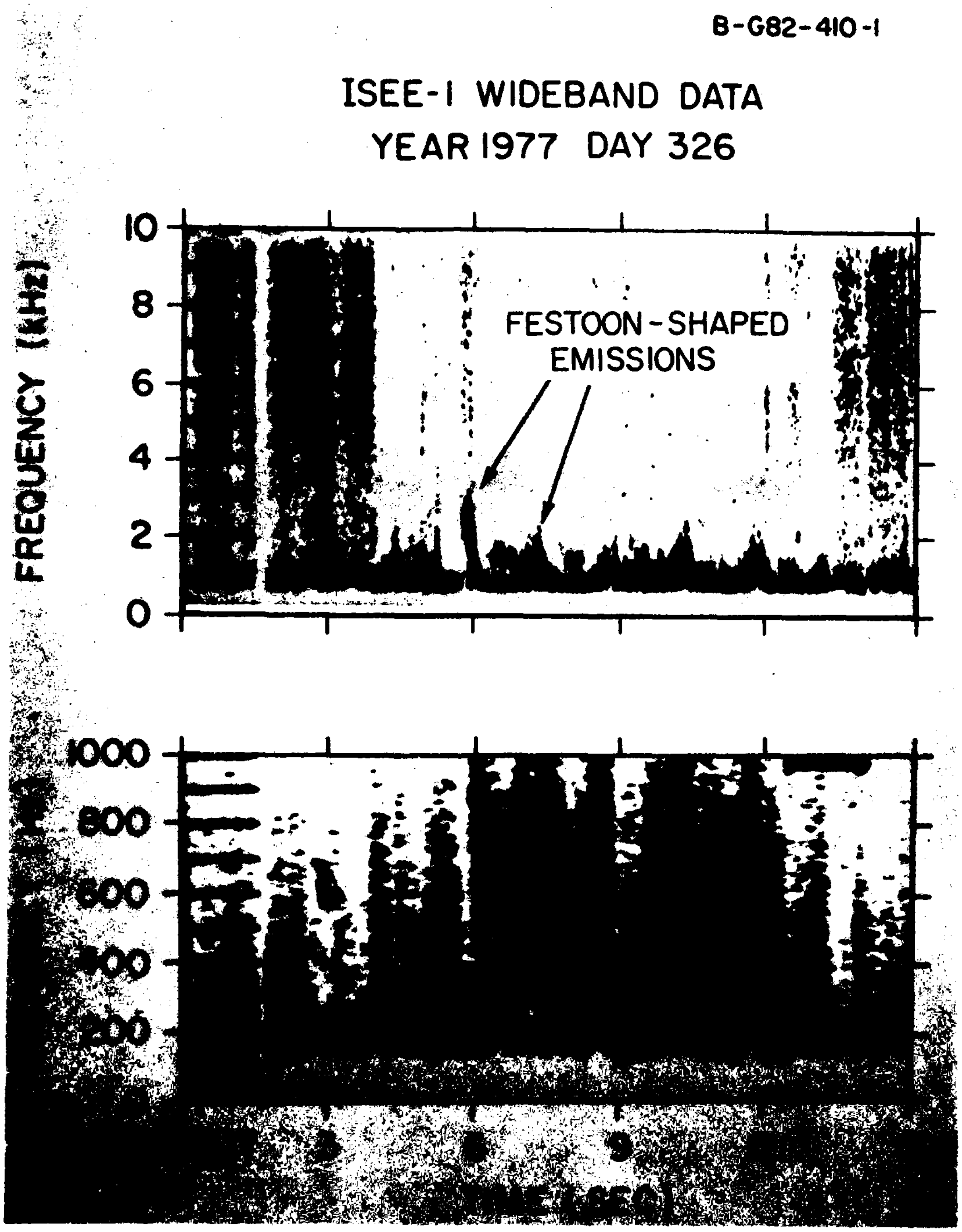
B-G82-410-1
ISEE-1 WIDEBAND DATA
YEAR 1977 DAY 326
FREQUENCY (kHz)
10
8
6
4
2
0
FESTOON-SHAPED
EMISSIONS
1000
800
600
400
200

Figure 2

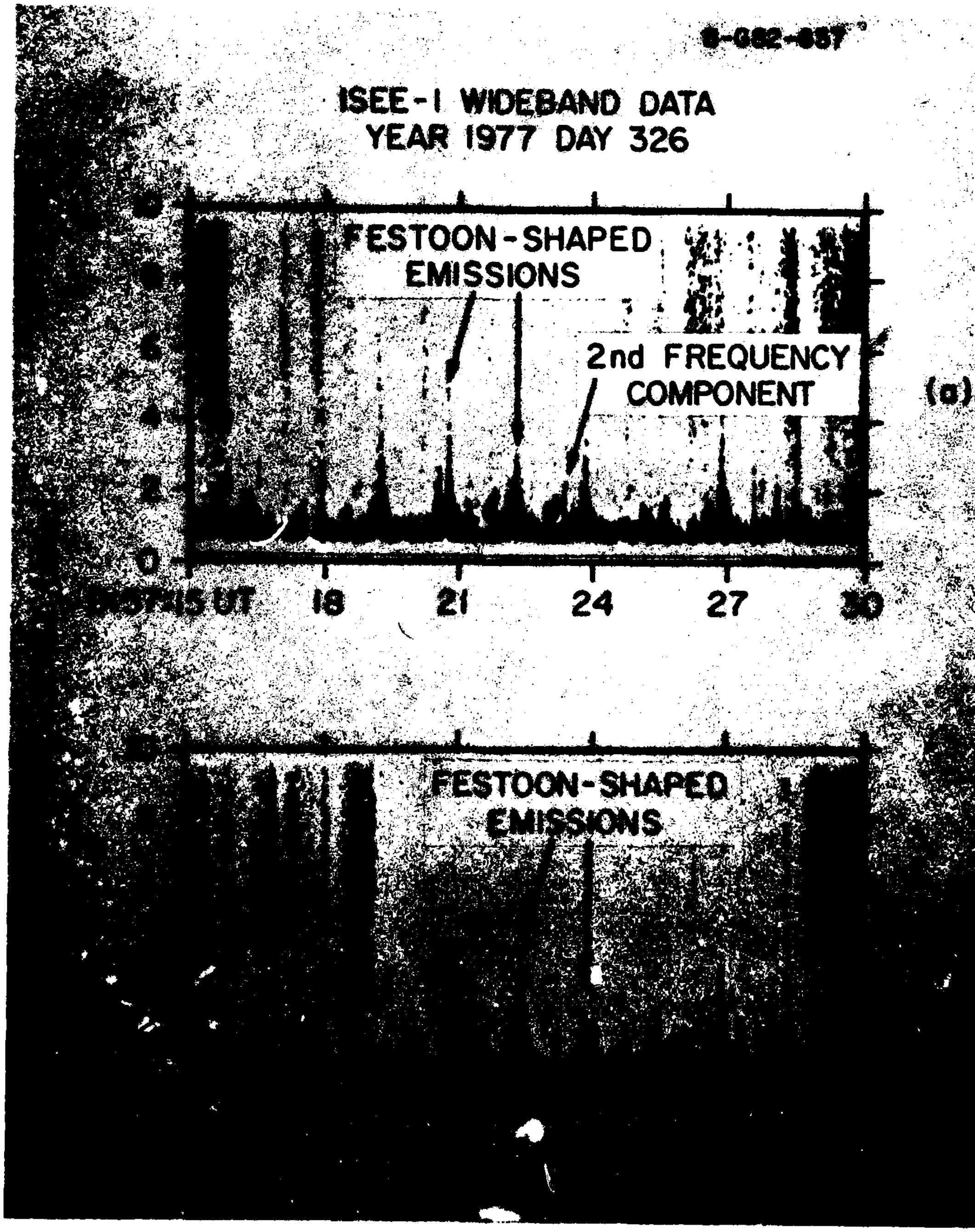
ISEE-1 WIDEBAND DATA
YEAR 1977 DAY 326
FESTOON-SHAPED
EMISSIONS
2nd FREQUENCY
COMPONENT
(a)
18
21
24
27
30
FESTOON-SHAPED
EMISSIONS

Figure 3

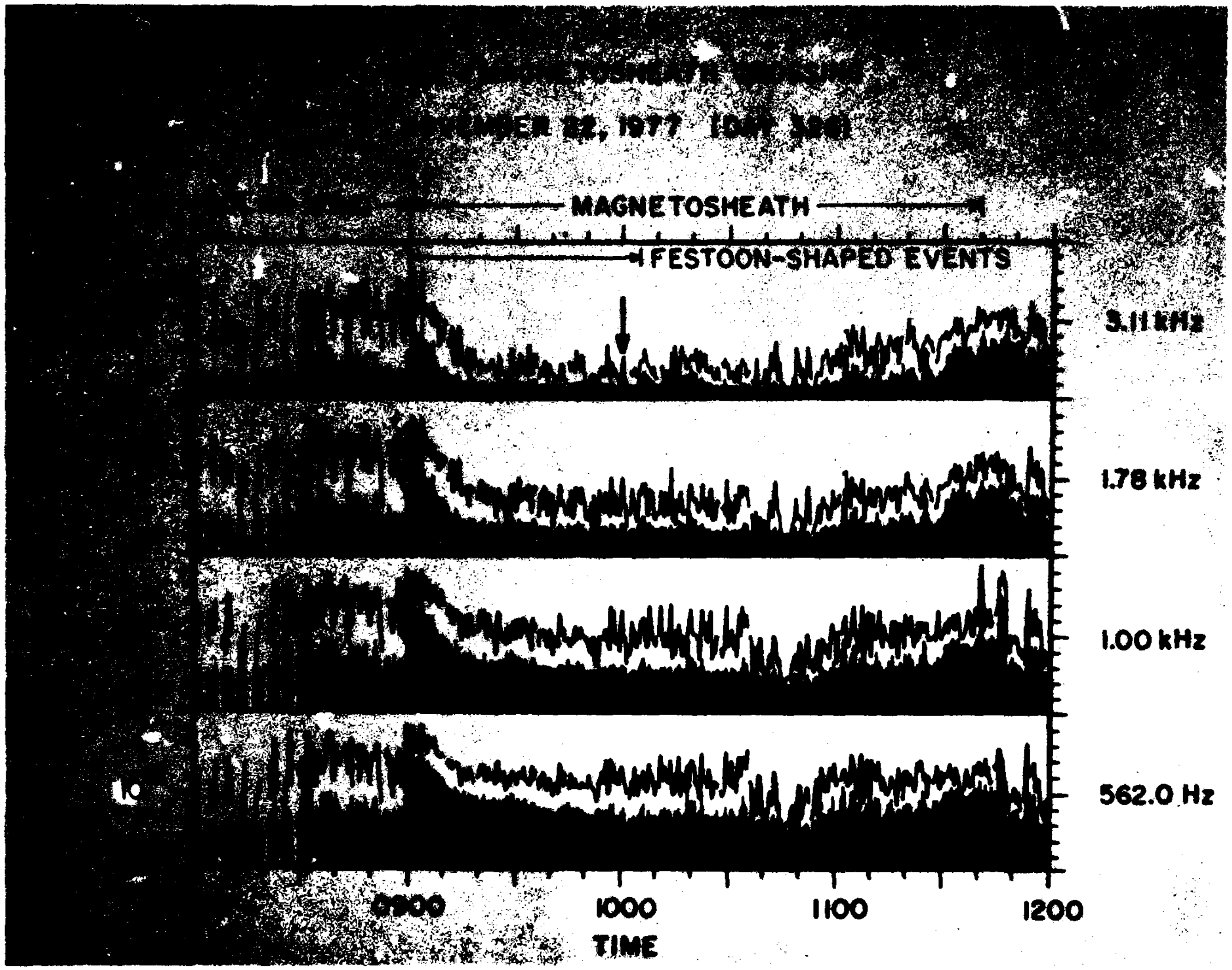
MAGNETOSHEATH
FESTOON-SHAPED EVENTS
3.11 kHz
1.78 kHz
1.00 kHz
562.0 Hz
1000
1100
1200
TIME

Figure 4

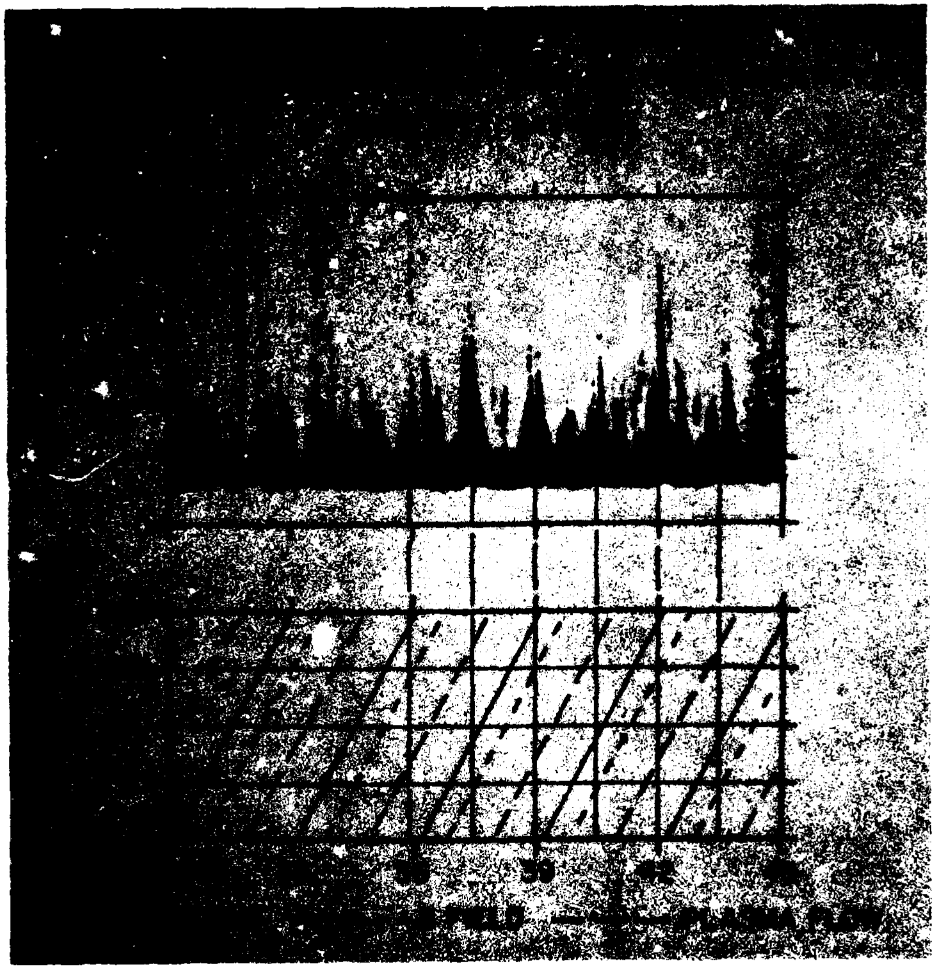

Figure 5

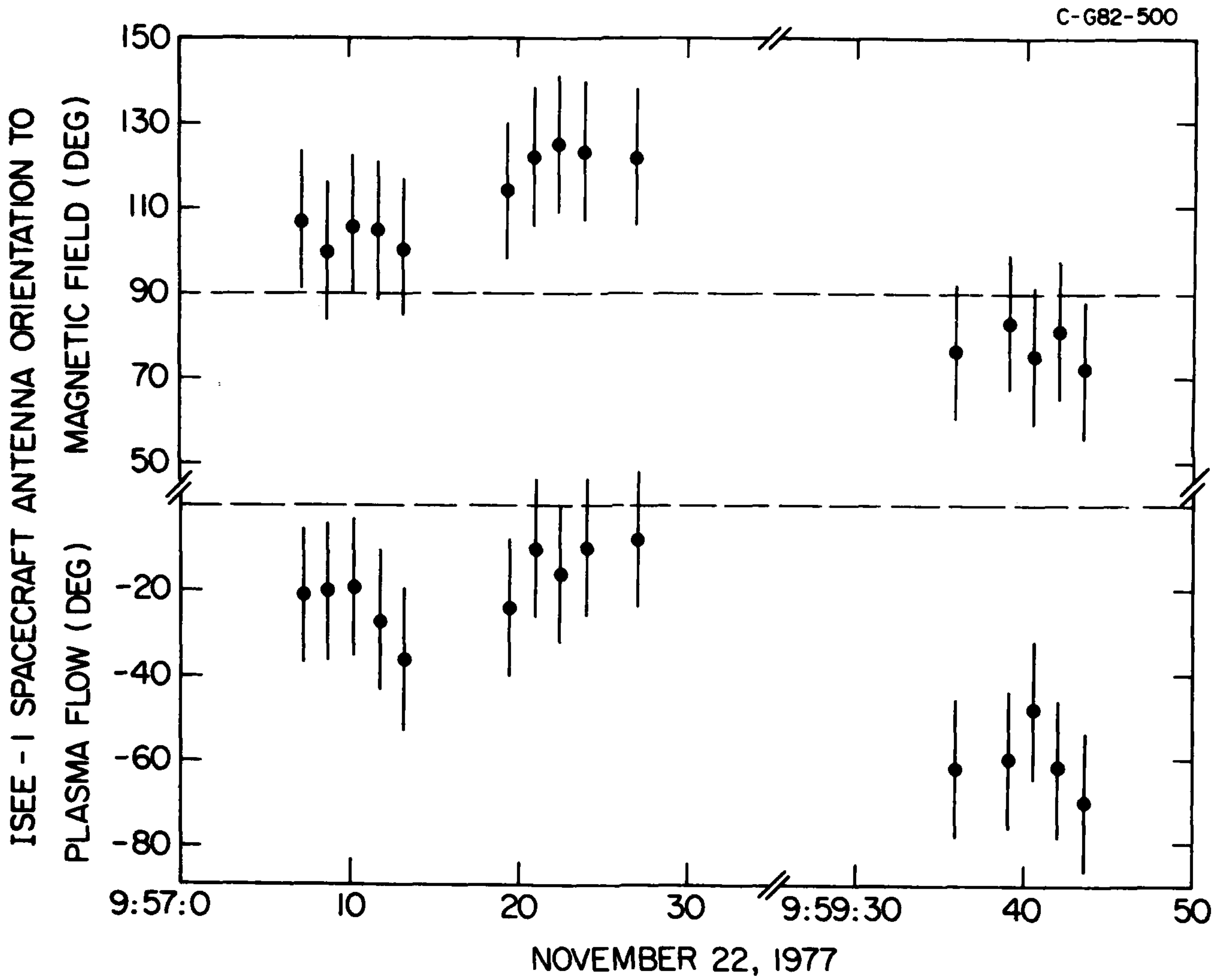
C-G82-500
ISEE - I SPACECRAFT ANTENNA ORIENTATION TO
MAGNETIC FIELD (DEG)
PLASMA FLOW (DEG)
150
130
110
90
70
50
-20
-40
-60
-80
9:57:0
10
20
30
9:59:30
40
50
NOVEMBER 22, 1977

Figure 6

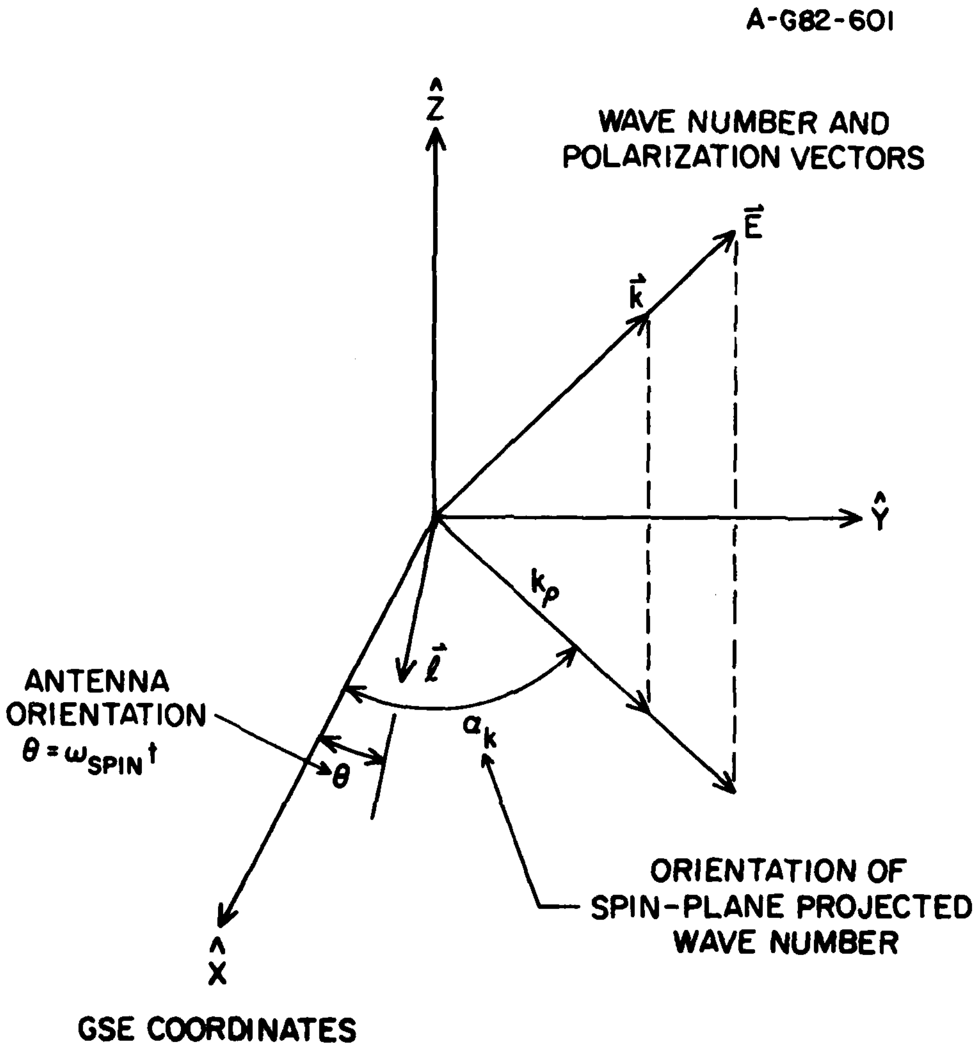
A-G82-601
WAVE NUMBER AND
POLARIZATION VECTORS
$\hat{Z}$
$\vec{E}$
$\vec{k}$
$\hat{Y}$
k_ρ
$\vec{\ell}$
ANTENNA
ORIENTATION
$\theta = \omega_{SPIN} t$
θ
α_k
ORIENTATION OF
SPIN-PLANE PROJECTED
WAVE NUMBER
$\hat{X}$
GSE COORDINATES

Figure 7

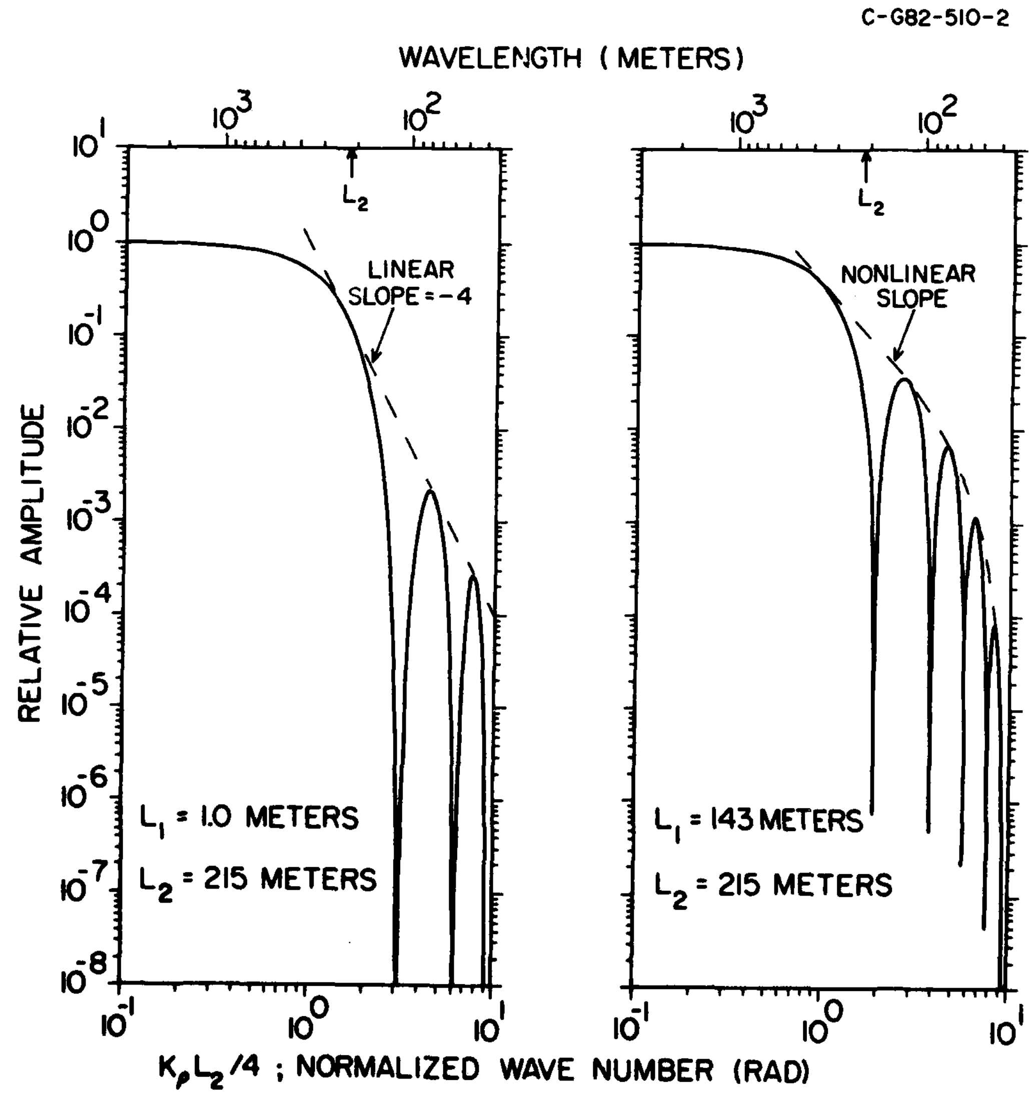
C-G82-510-2
WAVELENGTH (METERS)
10^3
10^2
L_2
LINEAR
SLOPE = -4
NONLINEAR
SLOPE
RELATIVE AMPLITUDE
L_1 = 1.0 METERS
L_2 = 215 METERS
L_1 = 143 METERS
L_2 = 215 METERS
K_ρL_2/4 ; NORMALIZED WAVE NUMBER (RAD)

Figure 8

A-G82-515-2

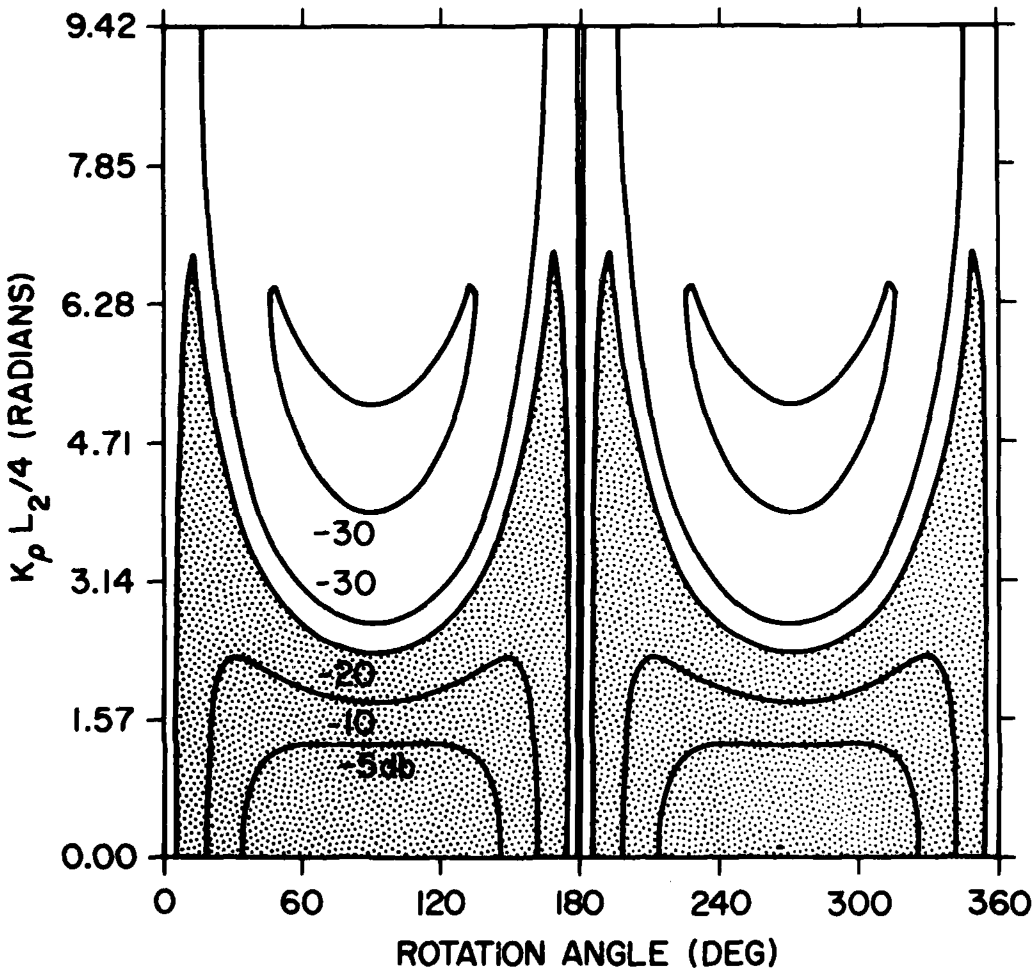

MODEL PARAMETERS
E-FIELD ANGLE = 90.0°
K-VECTOR ANGLE = 90.0°
ANTENNA LENGTH L1 = 1.0 METERS
ANTENNA LENGTH L2 = 215.0 METERS

Figure 9

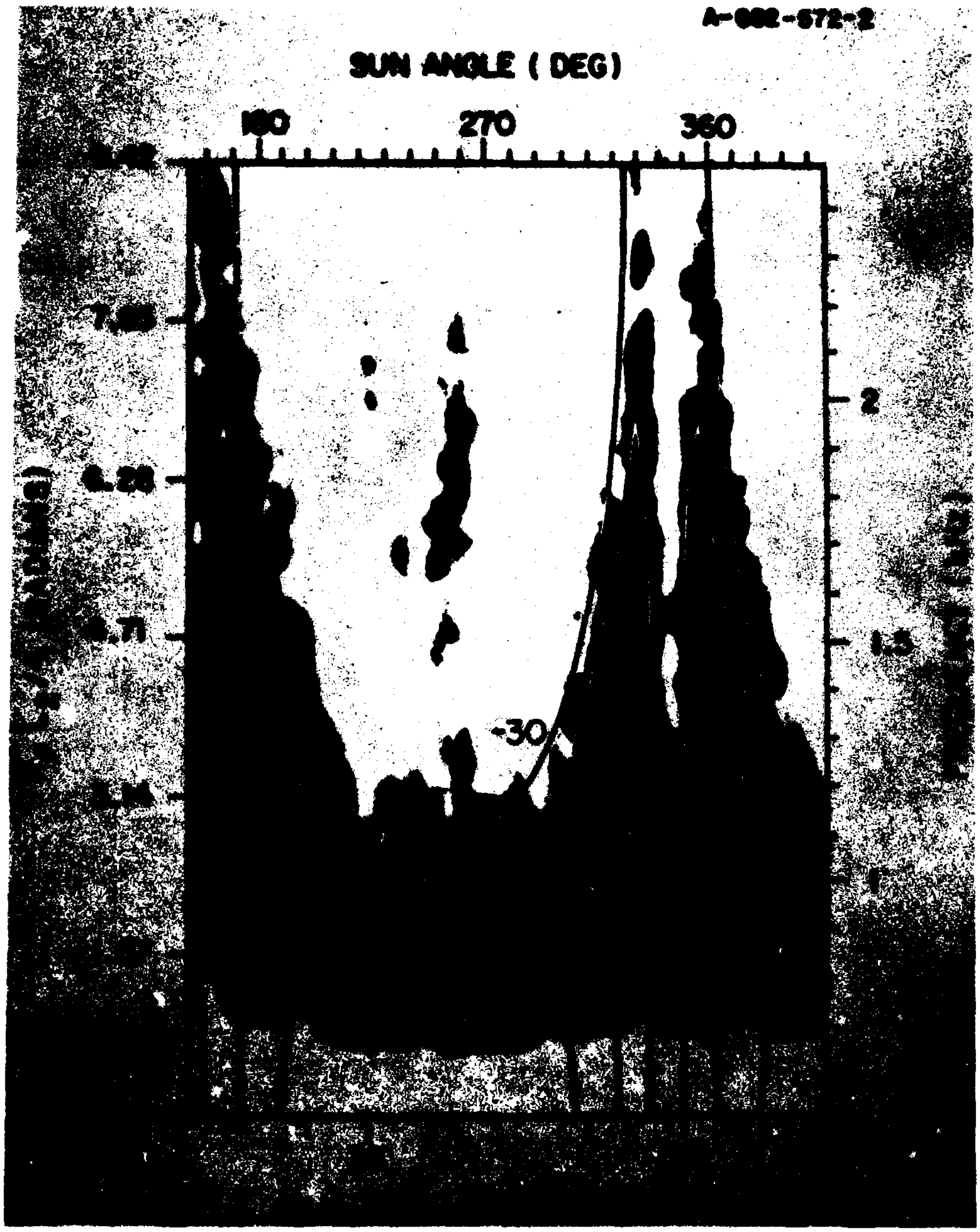

Figure 10

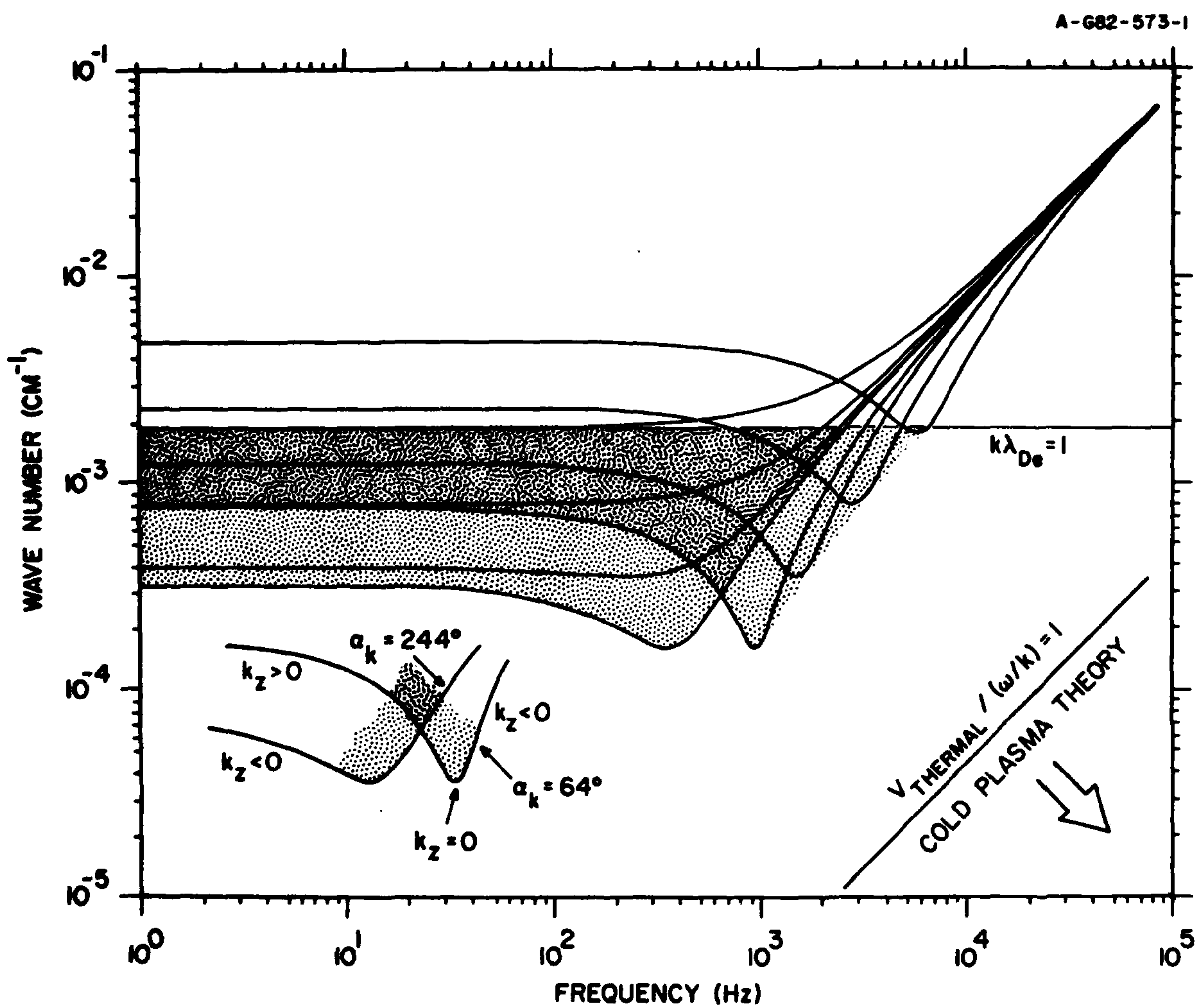

A-G82-573-1
WAVE NUMBER (CM^{-1})
10^{-1}
10^{-2}
10^{-3}
10^{-4}
10^{-5}
$k\lambda_{De} = 1$
$\alpha_k = 244°$
$k_z > 0$
$k_z < 0$
$k_z < 0$
$\alpha_k = 64°$
$k_z = 0$
$V_{THERMAL} / (\omega/k) = 1$
COLD PLASMA THEORY
10^0
10^1
10^2
10^3
10^4
10^5
FREQUENCY (Hz)

Figure 11

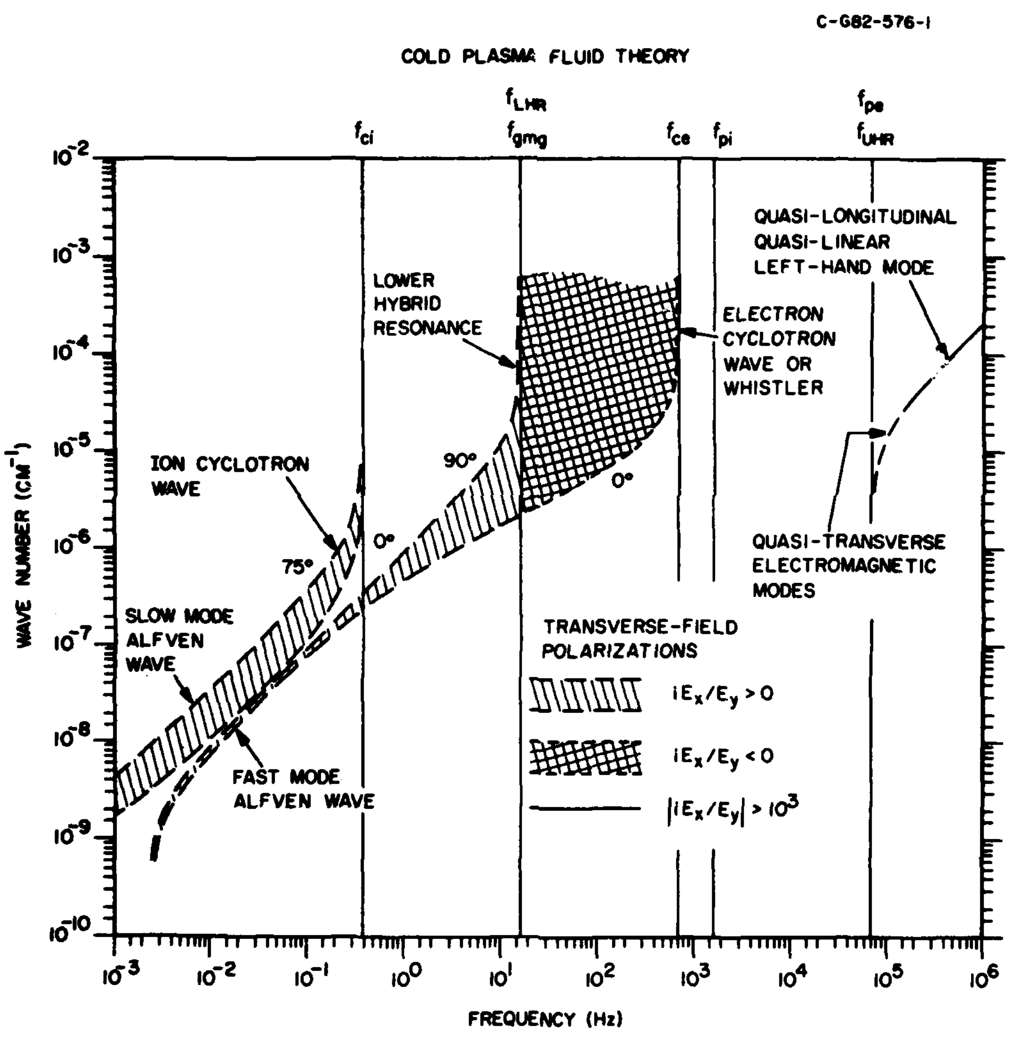

C-G82-576-1
COLD PLASMA FLUID THEORY
f_ci
f_LHR
f_gmg
f_ce
f_pi
f_pe
f_UHR
LOWER HYBRID RESONANCE
ELECTRON CYCLOTRON WAVE OR WHISTLER
QUASI-LONGITUDINAL QUASI-LINEAR LEFT-HAND MODE
QUASI-TRANSVERSE ELECTROMAGNETIC MODES
ION CYCLOTRON WAVE
SLOW MODE ALFVEN WAVE
FAST MODE ALFVEN WAVE
90°
0°
75°
0°
TRANSVERSE-FIELD POLARIZATIONS
iEx/Ey > 0
iEx/Ey < 0
|iEx/Ey| > 10^3
WAVE NUMBER (CM^-1)
FREQUENCY (Hz)

Figure 12

A-G82-580

EVENT GEOMETRY FOR
NOVEMBER 22, 1977 9^h 59^m $37.4^s - 39.4^s$

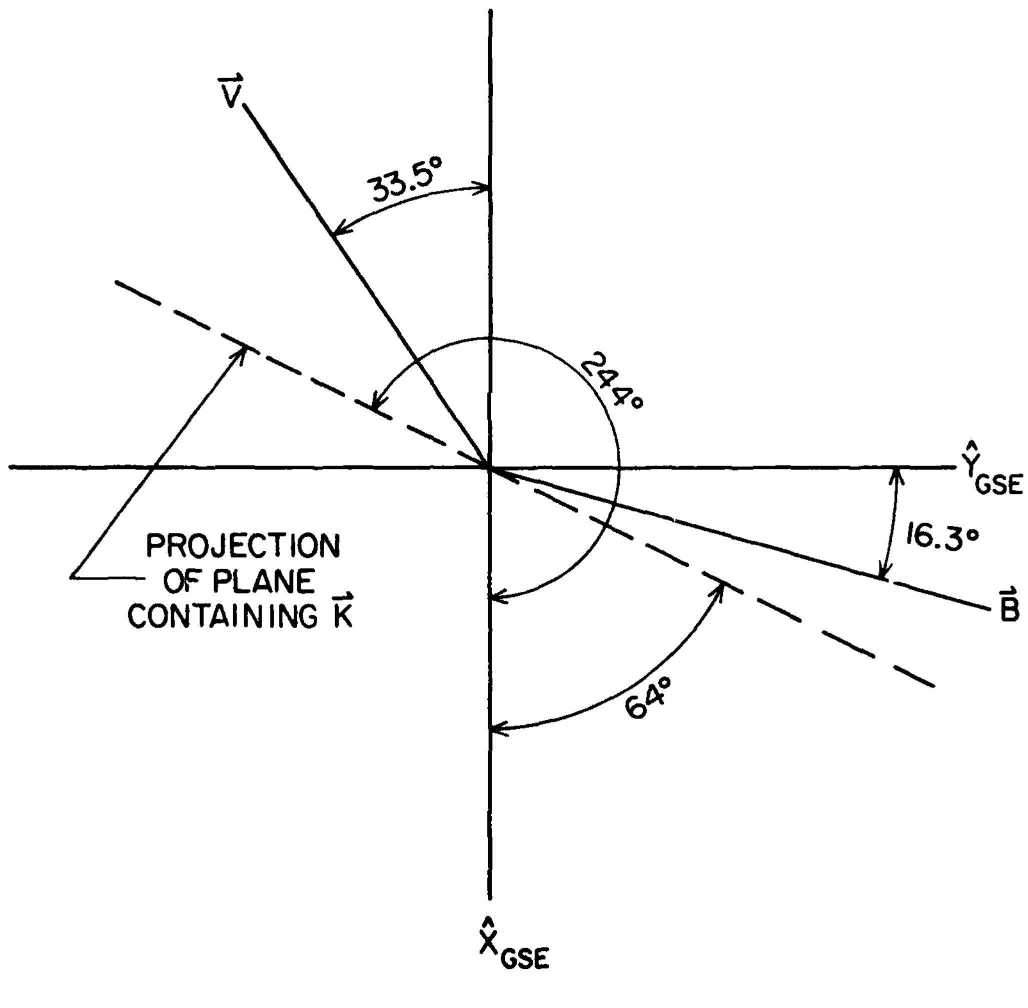

Figure 13

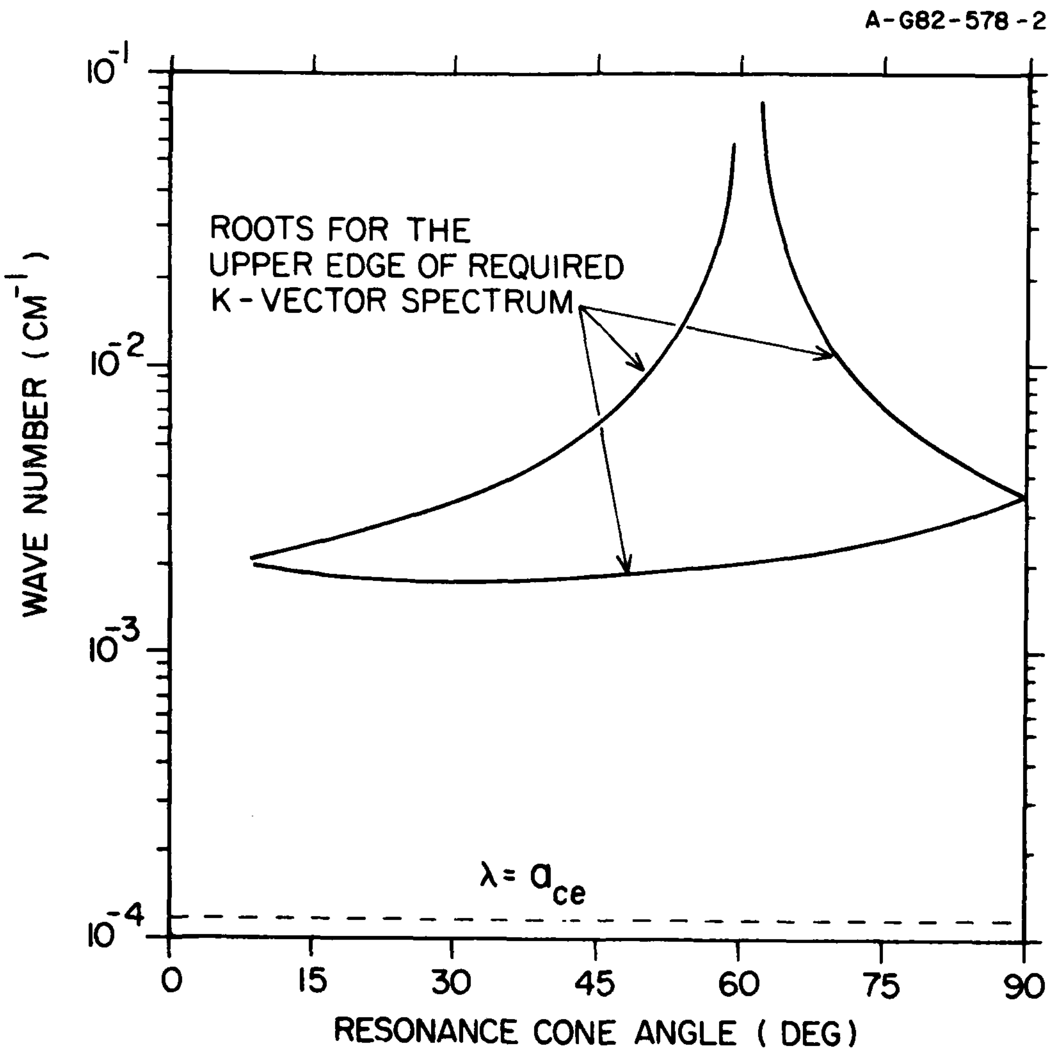
A-G82-578-2
ROOTS FOR THE
UPPER EDGE OF REQUIRED
K-VECTOR SPECTRUM
λ = a_ce
WAVE NUMBER (CM^-1)
10^-1
10^-2
10^-3
10^-4
0
15
30
45
60
75
90
RESONANCE CONE ANGLE (DEG)

Figure 14

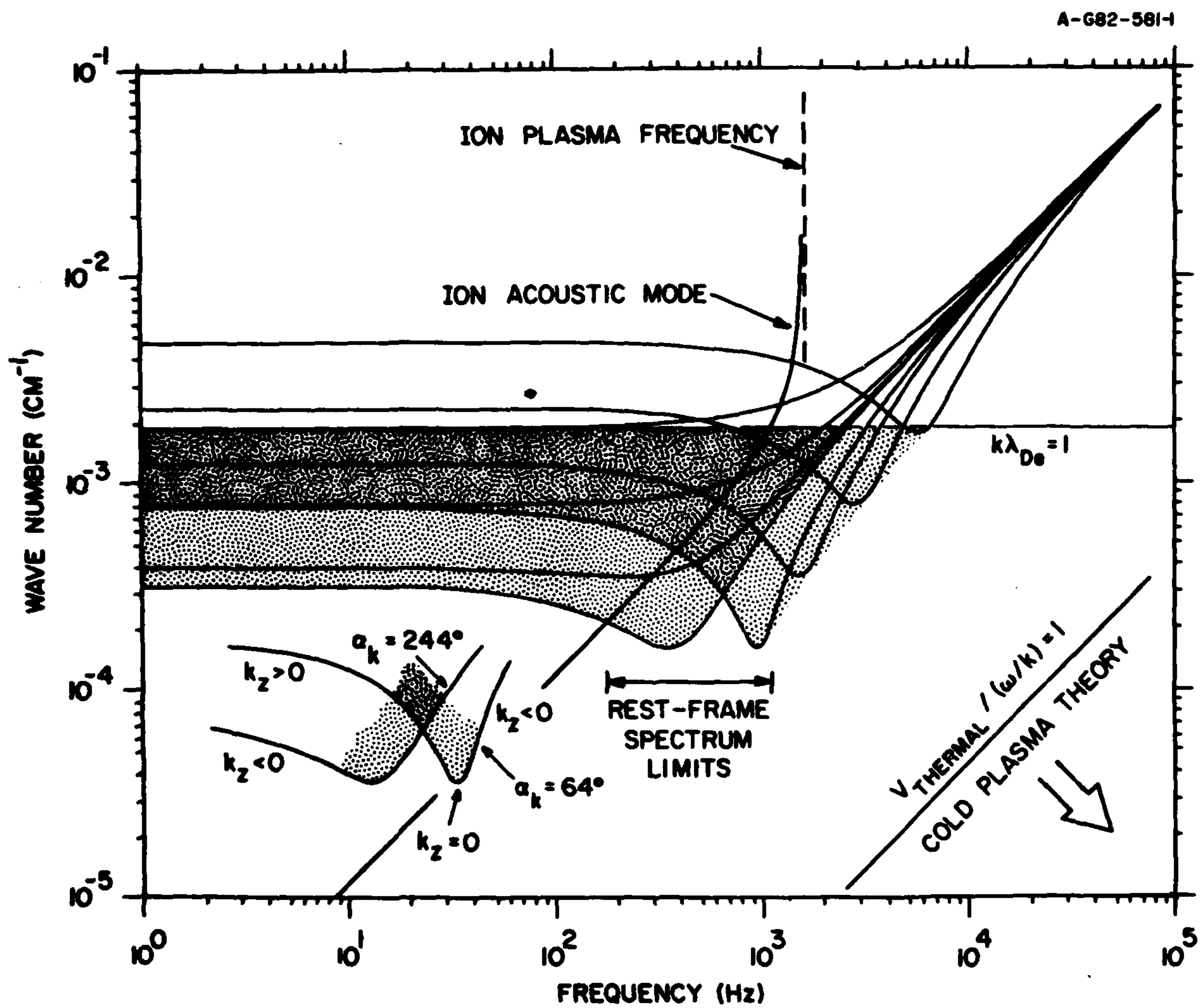
A-G82-581-1
ION PLASMA FREQUENCY
ION ACOUSTIC MODE
$k\lambda_{De}=1$
$\alpha_k = 244°$
$k_z>0$
$k_z<0$
$k_z<0$
$k_z=0$
$\alpha_k = 64°$
REST-FRAME
SPECTRUM
LIMITS
$V_{THERMAL} / (\omega/k) = 1$
COLD PLASMA THEORY
WAVE NUMBER (CM^{-1})
FREQUENCY (Hz)
10^{-1}
10^{-2}
10^{-3}
10^{-4}
10^{-5}
10^0
10^1
10^2
10^3
10^4
10^5

Figure 15

DATE
ILME